Ultrastructural sublaminar-specific diversity of excitatory synaptic boutons in layer 1 of the adult human temporal lobe neocortex

Astrid Rollenhagen[1*], Akram Sadeghi Dastjerdi[1*†], Bernd Walkenfort[2], Claus C. Hilgetag[3], Kurt Sätzler[4], Joachim HR Lübke[1,5,6]

[1]Institute of Neuroscience and Medicine INM-10, Research Centre Jülich GmbH, Leo-Brandt Str., 52425 Jülich, Germany; [2]Medical Research Centre, IMCES Electron Microscopy Unit (EMU), University Hospital Essen, Hufelandstr.11, 45122 Essen, Germany; [3]University Hospital Hamburg-Eppendorf, Center for Experimental Medicine, Institute for Computational Neuroscience, Martinistraße 52, 20246 Hamburg, Germany, [4]School of Biomedical Sciences, University of Ulster, Cromore Rd., BT52 1SA, Londonderry, UK; [5]Department of Psychiatry, Psychotherapy and Psychosomatics, Medical Faculty/RWTH University Hospital Aachen, Pauwelsstr. 30, 52074 Aachen, Germany; [6]JARA Translational Brain Medicine, Germany

*****both authors have equally contributed to the study

†**Present address:** Department of Anatomy and Molecular Neurobiology, University of Münster, Vesaliusweg 2-4, PAN-Center, 48149 Münster, Germany.

Address correspondence to: Joachim Lübke
Institute of Neuroscience and Medicine INM-10
Research Centre Jülich GmbH
52425 Jülich
Phone: +49-2461-612288
Fax: +49-2461-611778
E-mail: j.luebke@fz-juelich.de
Orchid ID: https://orcid.org/0000-0002-4086-3199

Abstract

Layer (L)1, beside receiving massive cortico-cortical, commissural and associational projections, is the termination zone of tufted dendrites of pyramidal neurons and the area of Ca^{2+} spike initiation. However, its synaptic organization in humans is not known. Quantitative 3D-models of synaptic boutons (SBs) in L1 of the human temporal lobe neocortex were generated from non-epileptic neocortical biopsy tissue using transmission electron microscopy, 3D-volume reconstructions and EM tomography. Particularly, the size of active zones (AZs) and the readily releasable, recycling and resting pool of synaptic vesicles (SVs) were quantified.

SBs had a single large AZ (~0.20 μm^2), a total pool of ~3500 SVs, a large readily releasable (~4 SVs), recycling (~470 SVs) and resting (~2900 SVs) pool. Astrocytic coverage suggests cross talk at synaptic complexes.

Thus, L1 SBs mediate, integrate and synchronize contextual and cross-modal information, enabling flexible and state-dependent processing of feedforward sensory inputs from other layers of the cortical column.

Key words: human neocortex, layer 1, synaptic complexes, quantitative 3D-models of synaptic boutons, astrocytic coverage, electron microscopy, EM tomography.

Introduction

The mammalian neocortex is the most complex part of the brain comprising over 75% of the gray matter. One fundamental feature established during development is the formation of distinct layers with different networks of neurons, and its organization into vertically oriented slabs, so-called cortical columns (Marin-Padilla 1978, 1998; reviewed by Rockland and DeFelipe 2018). This organization is established in an 'inside layers first-outside layers last' fashion (Luskin and Shatz 1985a, b; reviewed by Cooper et al. 2008). The exception, beside layer (L)6 is L1 generated first originating from the marginal zone (Marin Padilla 1998; reviewed by Bystron et al. 2008). Ongoing cortico- and synaptogenesis finally lead to the formation of the adult cortical network with its unique structural and functional properties (reviewed by Lübke and Feldmeyer 2007; Rockland and DeFelipe 2018).

Remarkably, L1 is highly conserved across cortical areas and higher mammalian species, but its importance was long underestimated. L1 is considered as the predominant input layer for top-down information, relayed by a rich, dense network of cortico-cortical, cortico-thalamic, commissural and associational long-range axonal projections. In humans, and thus different to experimental animals, both L1 excitatory Cajal-Retzius and a hetregeneous population of inhibitory neurons provide signals to the terminal tuft dendrites of pyramidal neurons of the underlying cortical layers. Thus, L1 is a central locus of neocortical associations controlled by distinct types of inhibition and feedforward excitation (Schumann et al. 2019; Hartung and Letzkus 2021, reviewed by Schumann et al. 2021).

The temporal lobe neocortex (TLN) is situated on the basolateral aspect of the cerebral hemispheres primarily observed in primates, including humans. Notably, in human, the TLN encompasses approximately 20% of the entire cerebral cortex (Kiernan 2012). It is recognized as a highly specialized associative neocortex, characterized by its homotypic granular six-layered organization (von Economo and Koskinas 1925; Palomero-Gallagher and Zilles 2019). The human TLN plays a crucial role in various cognitive functions, including auditory, visual, vestibular, linguistic, and olfactory processing. Additionally, it is intricately connected to diverse sensory and multimodal associational brain regions, such as the limbic system, amygdala, and various subcortical structures (Insausti 2013). Lastly, the human TLN serves as the epicenter and onset site for temporal lobe epilepsy (Allone et al. 2017; Tai et al. 2018).

One of the most important discoveries in neuroscience, beside the definition of the neuron by Cajal's

neuronal doctrine (1911), was the introduction of the term 'Synapse', more than 100 years ago. Since then these structures have been investigated from different viewpoints including structural, functional, molecular and computational studies summarized in meanwhile thousands of original publications, reviews and numerous textbooks. Yet, the quantitative geometry of the most prevalent synapse in the brain, the cortical synapse, has remained largely unexplored structurally, in both experimental animal models (but see Rollenhagen et al. 2015, 2018; Bopp et al. 2017; Hsu et al. 2017; Prume et al. 2020). and, even more so, in the context of the human brain (but see Yakoubi et al. 2019a, b; Dominguez-Alvaro et al. 2019, 2021; Cano-Astorga et al. 2021, 2023; Schmuhl-Giesen et al. 2022). This could be partially attributed to the availability of human brain tissue samples. Nevertheless, detailed and quantitative descriptions of synaptic complexes in L1 of the human brain are to date non-existing.

Here, an investigation into the synaptic organization of L1 in the human TLN was undertaken using high-resolution transmission electron microscopy (TEM), 3D-volume reconstruction to generate quantitative 3D-models of synaptic boutons (SBs) and by electron microscopic (EM) tomography. The ultimate objective of this comprehensive project is to elucidate the synaptic organization, layer by layer, of the cortical column in humans.

Such meticulous quantitative structural analyses of SBs and their corresponding target structures are indispensable for comprehending, elucidating, and establishing connections between the structural and functional properties of the diverse signal cascades underlying synaptic transmission, efficacy, strength, and plasticity. Consequently, these efforts contribute significantly to understanding the computational properties of brain networks, with the organization of the cortical column emerging as a pivotal component thereof.

Results

Synaptic density in L1a and L1b of the human TLN

Synaptic density measurements serve as a valuable tool for quantitatively characterizing the synaptic organization of a specific cortical layer, assessing the connectivity rate, and identifying potential inter-individual differences among patients within the human TLN.

The average density of synaptic complexes in L1 was comparatively high with a value of $5.26*10^8 \pm 8.44*10^7$, $5.52*10^8 \pm 1.86*10^7$ synapses/mm^3 in L1a and $3.93*10^8 \pm 1.35*10^7$ synapses/mm^3 in L1b, ranging from $3.9*10^8$ to $7.3*10^7$ (L1a) and from $2.6*10^8$ to $5.3*10^8$ (L1b), respectively (Source Data 1). Interestingly, the average synaptic density in L1a was by ~1.5-fold larger when compared with L1b although L1a was regarded as the more astrocytic dominated sublamina. Strikingly, a huge inter-individual variability was found, although with no significant difference between L1a and L1b.

Therefore, L1 exhibited a high density of synaptic complexes, indicating a relatively robust connectivity of neurons within L1 of the human TLN.

Neural and synaptic composition of L1 in the human TLN

L1 in the adult mammalian neocortex represent a relatively cell sparse layer that in humans can be subdivided into two sublaminae, L1a and L1b as revealed in Golgi-preparations, semithin sections (Figure 1A) and at the EM level (Figure 1H, I). L1a is dominated by a dense network of astrocytes of different shape and size, their fine processes (Figure 2A), the occurrence of reactive microglia (Figures 1H, I, 2A) and terminal tuft dendrites of pyramidal neurons throughout the neuropil of L1 (Figures 1H, I, 2B).

Hence, L1a can be characterized as a predominantly astrocytic sublamina, whereas L1b is primarily dominated by dendritic and synaptic profiles. Lipofuscin granules, indicative of aging, were frequently noted in astrocytes, reactive microglia (Figure 2A) and neurons, although their abundance, size, and morphology varied considerably.

Remarkably, and in contrast to rodents in humans a persistent subpopulation of CR-cells were found identifiable by the horizontal bipolar orientation of both dendrites and axons (Figure 1E-H). The majority were found directly underneath the pial surface (Figure 1F, G) or intermingled with a heterogeneous population of GABAergic interneurons (Figure 1E).

In the human TLN, GABAergic interneurons constitute the predominant class of neurons in L1, exhibiting significant structural heterogeneity, but structurally very heterogeneous class of neurons in L1 (Figure 1D, E; see also Verhoog et al. 2016; Schuman et al. 2019, reviewed by Schuman et al. 2021) which

were found throughout both sublaminae and were sometimes organized in clusters of 3-6 neurons (Figure 1D).

Beside CR-cells and GABAergic interneurons, also degenerating neurons, identifiable by their shrunken and dark appearance (Figure 1A, I) were found in both sublaminae although their numbers varied substantially between brain tissue samples.

While L1a is primarily characterized by the presence of astrocytes and their fine processes, it also harbors numerous synaptic complexes. These complexes consist of a SB juxtaposed with either a dendritic shaft or spine (Figure 2A) directly beneath or interwoven among the fine astrocytic processes within L1 (Figure 2A).

In contrast, L1b is a more 'dendritic and synaptic layer' due to a massive increase in synaptic complexes (Figures 1H, 2B). Furthermore, L1b is infiltrated by apical dendrites of L2, L3 and L5 pyramidal neurons which are interspersed with smaller dendritic segments representing apical oblique dendrites (Figures 1I, 2B). The majority of synaptic complexes were axo-spinous (~80%, Figure 2 B, D, E), the remainder were axo-dendritic some of which but not all were regarded as putative GABAergic terminals (Figure 2C).

L1b can be separated from L2 by the sudden increase of neuronal cell bodies and thick apical dendrites originating at the upper pole of the somata of pyramidal neurons (Figures 1A, 2B). At the L1b and L2 transition more and more apical and apical oblique dendrites of different caliber were observable.

Synaptic organization of L1 in the human TLN

The primary objective of this study was to explore the synaptic organization of L1 in the human TLN, focusing on synaptic parameters that represent morphological indicators of synaptic transmission, efficacy, strength and plasticity. The quantitative analysis was conducted separately for both sublaminae to identify potential sublaminar-specific differences. The quantitative analysis was separated for both sublaminae to look for possible sublaminar-specific differences. Beside the overall geometry of SBs and the number and size of mitochondria, in particular the size of the PreAZ and PSD constituting the AZ, the morphological

equivalent to a functional neurotransmitter release site and the organization of the three pools of SVs, namely the readily releasable (RRP), the recycling (RP) and resting pool, were quantified.

To achieve this, a total of 361 SBs was completely reconstructed out of four patients in six series containing 100-150 ultrathin sections/series. A total of 190 SBs and 184 AZs (L1a) and 171 SBs and 165 AZs (L1b) using non-affected neocortical access tissue (see Material and Methods; Source Data 2) were completely 3D-reconstructed and quantified using file-scale TEM and subsequent 3D-volume reconstructions.

Excitatory and inhibitory synaptic complexes in L1a und L1b were formed by either presynaptic *en passant* or endterminal boutons with their prospective postsynaptic target structures dendritic shafts (Figures 2B C, D, 3A-C) or spines of different caliber and type (Figures 2B, D, E, 3A-C). In both sublaminae, SBs were predominantly found on dendritic spines (~81%; L1a) and ~79% (L1b), the remainder were located on dendritic shafts. SBs on spines were predominantly located on mushroom spines (L1a: ∼83%, L1b: ∼73%), a smaller fraction on stubby spines (L1a: ∼11%, L1b: ∼9%) or on thin elongated spines;(L1a: 6%, L1b: ∼22%; Figure 2E), the remainder were not classifiable.

Numerous SBs in both sublaminae were seen to establish either two or three synaptic contacts on the same spine or dendrite. Infrequently, GABAergic synapses identified by the smaller more spherical SVs and glutamatergic terminals were found on the same dendrite (Figure 2C, D) or spine. Remarkably, ~90% of spines in L1a and L1b contained a spine apparatus (Figure 2E), a specialized form of the endoplasmic reticulum, structures that increase spine motility and may also stabilize the synaptic complex during signal transduction (Deller et al. 2003; reviewed by Knott and Holtmaat 2008).

In numerous SBs, so-called dense-core vesicles (DCWs) were distributed throughout the presynaptic terminal intermingled with the population of SVs (Figure 3B, C, E).

Remarkably, beside synaptic complexes, also ‘special connections’ in L1 of the human TLN were observed. This encompassed so-called dendro-dendritic synapses and fine astrocytic processes that receive synaptic input from SBs and in turn, provide synaptic output to either dendritic shafts or spines (not shown, but see Yakoubi et al. 2019a, b: Schmuhl-Giesen et al. 2022),

Geometry and size of SBs and mitochondria in the human TLN

Overall, L1 SBs were on average medium-sized, with a mean surface area of 5.48 ± 1.40 µm^2, and a mean volume of 0.50 ± 0.19 µm^3, with a slight difference in size between L1a and L1b. Interestingly, the variability in both surface area and volume of SBs was comparably small in L1a and L1b as indicated by a low CV and variance (Table 1; Source Data 2) regardless of their target structures. SBs in L1 were comparable in size with SBs in L5, L6, but ~2-fold larger than those in L4 of the human TLN ($p \leq 0.001$; see also Yakoubi et al. 2019a, b: Schmuhl-Giesen et al. 2022),)

Mitochondria play a pivotal role in synaptic transmission and plasticity (reviewed by Dallerac et al. 2018). In L1 SBs either no (Figures 2B, 3A, E) or several mitochondria (Figures 2, 3C, D; range 0 to 8) of different shape and size were observed. Mitochondria had a volume of 0.04 ± 0.02 µm^3 in L1a and 0.05 ± 0.01 µm^3 in L1b, respectively (Table 1; Source Data 2). Mitochondria contributed with ~7% (L1) to the total bouton volume, similar to values in L6 (~6%; Schmuhl-Giesen et al. 2022), but with ~1.5-fold lower percentage as those in L5 (~12%; Yakoubi et al. 2019a) and L4 (~13%; Yakoubi et al. 2019b).

A good correlation between the volume of the SBs and that of mitochondria was found for L1a (R^2: 0.7528; Figure 4B) and for L1b (R^2: 0.5992; Figure 4B). A weak correlation was also found for L6 (Schmuhl-Giesen et al. 2022) but a strong one in both L4 (Yakoubi et al. 2019a) and L5 (Yokoubi et al. 2019b) suggesting a layer-specific difference in the content of mitochondria in individual SBs.

Structural composition of AZs in L1a and L1b excitatory SBs in the human TLN

The number, size, and shape of the AZ, composed of the PreAZ and PSD, is one key structural determinant in synaptic transmission and plasticity (Südhof 2002; Matz et al. 2010; Holderith et al. 2012) as it represents the docking area of SVs (PreAZs) and the receiving area of neurotransmitter quanta (PSD) (Südhof 2012).

The majority (~98%) of SBs in L1a and L1b had only a single (Figures 2C-E, 3A-C, E) at most two or three AZs (Figure 3D, D). Beside very large, spanning the entire pre- and postsynaptic apposition zone, also smaller AZs covering only a fraction of the pre- and postsynaptic apposition zone were found. The majority

of AZs (~75%) were of the macular, non-perforated type (Figures 2C-E, 3A-D), the remainder showed either a perforation in the PreAZ, PSD or both (Figure 3E).

On average, PreAZs were 0.18 ± 0.08 μm^2 in surface area in L1a and 0.22 ± 0.04 μm^2 in L1b with only a slight variability between both sublaminae. The surface area of PSDs was 0.21 ± 0.01 μm^2 in L1a and 0.22 ± 0.05 μm^2 in L1b, respectively (Table 1; Source Data 2). The similar size of the PreAZ and PSD showed a nearly perfect overlap at the pre- and postsynaptic apposition zone. L1 AZs did not show a large variability in size as indicated by the low SD, CV, and variance (Table 1).

Notably, our analysis revealed only a weak correlation between the surface area of SBs and that of PreAZs for L1a and L1b SBs (Figure 8A). These findings imply that the size of SBs and PreAZs is independently regulated from each other.

The width of the synaptic cleft (Table 1; Source Data 2) is an important measure at AZs since its size (diameter) critically determines the temporal and spatial neurotransmitter concentration. The cleft widths were slight, but non-significantly different between the two sublaminae and similar to findings in L4, L5 and L6 (Yakoubi et al. 2019a, b: Schmuhl-Giesen et al. 2022).

Organization of the pools of SVs in L1a and L1b excitatory SBs of the human TLN

SVs are the other key structure in neurotransmitter storage and release, hence they play a fundamental role in synaptic transmission and in the modulation of short- and long-term synaptic plasticity (Südhof 2002, 2012) Three different pools of SVs are functionally defined: the RRP, the RP, and the resting pool. Synaptic efficacy, strength, mode, and probability of release (P_r) are regulated by these pools (Schikorski and Stevens 2001; Silver et al. 2003; Rizzoli and Betz 2004; Saviane and Silver 2006; Schikorski 2014; Watanabe et al. 2014; Neher 2015; Vaden et al. 2019; reviewed by Rizzoli and Betz 2005; Denker and Rizzoli 2010; Chamberland and Toth 2016)

In general, SVs were distributed throughout the entire terminal in ~95% of the population of SBs investigated (Figure 2, 3), the remainder showed a more cluster-like distribution. Two different types of vesicles were found: (1) Small clear SVs with an average diameter of 25.03 ± 5.27 nm (Table 1; Source

Data 2) and (2) DCVs (Figure 3B, C, E; Source Data 2) with an average diameter of 57.97 ± 6.45 nm with no significant difference between both sublaminae. DCVs were intermingled with the population of SVs throughout the entire SB (Figure 3B, C, E).

DCVs play an important role in endo- and exocytosis build-up of PreAZs by releasing Piccolo and Bassoon (Schoch and Gundelfinger 2006; Murkherjee et al. 2010), or in clustering SVs at the PreAZs (Watanabe et al. 2014, Murkherjee et al. 2010). In addition, various co-transmitters, such as neuropeptides, ATP, noradrenalin, and dynorphin were identified in large DCVs (Ghijsen and Leenders 2005).

The distribution pattern of SVs made it impossible to morphologically distinguish between the three functionally defined pools of SVs, except for the so-called 'docked' and fused vesicles primed to the PreAZ (Rizzoli and Betz, 2004; Neher 2015; reviewed by Rizzoli and Betz 2005; Chamberland and Toth 2015).

Thus, a perimeter analysis (a modified Sholl-analysis) was used to determine the exact location of each SV from the PreAZ in individual terminals (for criteria to define SV pools see Rizzoloi and Betz 2005). The RRP were defined as a distance (perimeter p) from ≤10 nm and ≤20 nm from the PreAZ. This criteria for the RRP was chosen because both values are less than an SV diameter and hence may represent the RRP from which SVs could be easily and rapidly recruited. The RP maintains release during moderate stimulation and was estimated close (p60-p200 nm) to the PreAZ. All SVs further than 200 nm from the PreAZ constituted the resting pool which acts as a deposit of SVs only used by intense and/or repetitive stimulation.

The average total pool of SVs was 2958.62 ± 1940.51 in L1a vs. 3903.32 ± 1852.23 in L1b with an average of 3430.97 ± 1773.77 for L1 (Table 1; Source Data 2). Remarkably, the total pool in L1b was significantly larger ($p \leq 0.01$) by ~1.3-fold when compared to L1a although a huge variability in total pool size exists in both sublaminae (Figure 3D, E) ranging from 758 to 6542 in L1a and 1507 to 15060 in L1b as indicated by the SD, IQR and variance (Table 1). SVs contributed with ~5% (0.03 μm^3) in L1a and ~4% (0.02 μm^3) in L1b to the total volume of SBs, however, with no significant difference between both sublaminae (Table 1; Source Data 2).

Interestingly, no correlation between the volume of SBs vs. the total pool size was found for L1a (R^2: 0.2490), but a good correlation was observed for L1b (R^2: 0.5700). Furthermore, no correlation was found between the PreAZ vs. the total pool size (Figure 4C; Source Data 2).

The average RRP/PreAZ for L1was 3.60 ± 4.24 SVs at p10 nm (L1a: 5.90 ± 5.05 SVs and L1b: 1.29 ± 1.87 SVs) with a significant difference ($p \leq 0.01$) by ~4.5-fold between the two sublaminae (Table 1; Source Data 2). The RRP/PreAZ at p20 nm criterium was on average 19.05 ±17.23 SVs (L1a: 25.04 ± 21.09 SVs and L1b: 13.07 ± 13.87SVs) and thus nearly 2-fold larger for L1a. Interestingly, both RRPs in L1a and L1b were characterized by a comparably low variability as indicated by the SD, CV, and variance (Table 1) pointing to sublamina-specific differences in P_r, synaptic efficacy, strength and paired-pulse behavior at individual SBs. No correlation between the RRP at both the p10 nm and p20 nm criterium and the surface area of PreAZs was found for both sublaminae. (Figure 4D, E).

The RP/PreAZ at 60-200 nm perimeter criterium was 390.12 ± 286.89 SVs in L1a and 535.88 ± 321.16 in L1b with no significant difference for both sublaminae (Table 1; Source Data 2). It should be noted however, that the variability of the RP is relatively large in both sublaminae as indicated by the SD, median, IQR and variance (Table 1).

No correlation was observed between the SVs in the p60-200 nm RP and the surface area of the PreAZs (L1a, Figure 4F) and for L1b (Figure 4F; Source Data 2), respectively.

The resting pool of SVs contained on average 2515.02 ± 1588.99 SVs in L1a and 3277.97 ± 1480.96 SVs in L1b with a significant difference between the two sublaminae ($p \leq 0.01$, Table 1; Source Data 2). The number of SVs in the resting pool in L1b was about 1.3-fold larger when compared to L1a. Again, also the resting pool showed a large variability for both sublaminae as indicated by the SD, CV, IQR and variance (Table 1).

No correlation was observed between the SVs in the p200 nm and p500 nm resting pool and the surface area of the PreAZs in L1a and L1b (Figure 4G, H; Source Data 2).

EM tomography of L1 excitatory SBs in the human TLN

It is still controversially discussed whether so-called ‘docked’ SVs represent the RRP. To compare our results from the perimeter analysis for the p10 nm RRP with that of ‘docked’ SVs, high-resolution EM tomography was carried out. Only SBs where the AZ could be followed from its beginning to its end in individual tilt-series and where the AZ was cut perpendicular through the PreAZ, PSD and the synaptic cleft were analyzed. In L1a (50 SBs, on shafts = 25 SBs; on spines = 25 SBs) and L1b (50 SBs on shaft = 25 SBs; on spines = 25 SBs) the number of ‘docked’ SVs was analyzed at the PreAZ (Figure 5; Table 2; Source Data 3).

The results for L1a and L1b were two-fold: First, and in agreement with already published results (Yakoubi et al. 2019a, b; Schmuhl-Giesen et al. 2022) only in a minority (<1%) of all PreAZs analyzed, regardless of their target structures, a dendritic shaft (Figure 5A) or spine (Figure 5B, C), no ‘docked’ SVs were observed. Second, the majority of PreAZs (~98%) contained more than 2, the most 8 (L1a) and 6 (L1b) ‘docked’ SVs. This finding strongly supports multivesicular release of ‘docked’ SVs in L1a and L1b SBs in line with findings in L4, L5 and L6 SBs (Yakoubi et al. 2019a, b; Schmuhl-Giesen et al. 2022; see also Figure 5D-F).

On average, 3.71 ± 1.38 ‘docked’ SVs (L1a) and 3.42 ± 1.34 ‘docked SVs’ (L1b) were found at individual PreAZs with similar values for both sublaminae. Furthermore, no significant difference was found for ‘docked’ SVs between shaft vs. spine synapses in L1 ($p < 0.001$). Strikingly, the number of ‘docked’ SVs at L1a PreAZs was ∼2-fold smaller but ~3-fold larger in L1b when compared to the results of our quantitative perimeter analysis for the p10 nm criterion and were also significantly different ($p < 0.001$). The number of ‘docked’ SVs showed a relatively low variability as indicated by the SD, CV, variance, and skewness, but were different from the values estimated with the p10 nm perimeter analysis. There seems to be a tendency that larger PreAZs contained more ‘docked’ SVs providing a larger ‘docking’ area allowing the recruitment of more SVs.

In summary, a notable disparity difference was observed between values obtained for L1 using the p10 nm criterion of the perimeter- and the EM tomography analysis. Additionally, the RRP in L1 and L6 was

~2-4-times smaller when compared to values in L4 and L5 (Yakoubi et al. 2019a, b; Schmuhl-Giesen et al. 2022) pointing towards a layer-specific regulation of the RRP.

Astrocytic coverage of L1 SBs in the human TLN

Astrocytes, by directly interacting with synaptic complexes forming the 'tripartite' synapse play a pivotal role in the induction, maintenance and termination of synaptic transmission by controlling the spatial and temporal concentration of neurotransmitter quanta in the synaptic cleft (reviewed by Dellarac et al. 2018). Astrocytes and their fine processes formed a relatively dense but comparably loose network within the neuropil in L1a and L1b (Figure 6A, B). However, and in contrast to L2, L3, L4 and L5 but similar to findings in L6 of the human TLN synaptic complexes in L1 were only partially ensheated by fine astrocytic processes that physically isolate synaptic complexes from the surrounding neuropil (Figure 6A, B). In only a small fraction, fine astrocytic processes were observed to form the 'tripartite' synapse. Moreover, the percentage (mean ± SD) of the volumetric fraction of astrocytic processes to the total volume revealed a lower, although not significantly different, amount of astrocytic processes in L1 compared to L2-L5, but comparable to L6 (Figure 6C; Source Data 4).

Hence, it is most likely that the partial coverage or complete absence of fine astrocytic processes at the majority of synaptic complexes in L1 of the human TLN may contribute to different 'behaviors' of synaptic complexes, for example in the removal of 'spilled' horizontally diffusing neurotransmitter quanta favoring synaptic crosstalk (for more detail see Discussion).

Discussion

This study investigated the synaptic organization of L1 in the human TLN. The quantitative 3D-models analyzed showed beside similarities significant layer-specific differences in those structural and synaptic parameters, in particular in the size of the AZ and the total pool of SVs, the RRP, RP and resting pool when compared with other already investigated layers (Yakoubi et al. 2019a, b, Schmuhl-Giesen et al. 2022). The

low degree of astrocytic coverage of L1 SBs suggests that glutamate spillover and as a consequence synaptic cross talk may occur at the majority of synaptic complexes in L1.

Synaptic density measurements

Synaptic density measurement are a useful tool to describe the synaptic organization of a particular area, nuclei and even layers in different brain regions, but also the degree of connectivity underlying the computational properties of a given brain area or in a given brain network. Meanwhile numerous studies in various animal species and brain regions have performed such an analysis but data for a density of synaptic complexes in humans are still rare (but see Marco and DeFelipe 1998; Tang et al. 2001; DeFelipe et al. 1999, 2002; Alonso-Nanclares et al. 2008; Blazquez-Llorca et al. 2013; Finnema et al. 2016; Cano-Astorga et al. 2021, 2023).

Strikingly, a huge layer-specific difference in the mean density of synaptic contacts was found in the human TLN. In L1, the overall density was $5.26 \pm 8.44*10^8$ synaptic complexes/mm^3 although a great variability was observed as indicated by the SD larger than the mean consistent with findings in the other layers of the human TLN L5 ($3.89 *10^8 \pm 9.12*10^8$; Yakoubi et al. 2019a); L4 ($2.37*10^6 \pm 2.19*10^6$; Yakoubi et al. 2019b), and L6 ($4.98 \pm 2.19*10^6$; Schmuhl-Giesen et al. 2022) and existing data published by Alonso-Nanclares et al. 2008: $9.13 \pm 0.63*10^8$ and Tang et al. 2001: $164*10^{12}$. The density values for L1 and L5 are in the same order of magnitude but differed substantially for L4 and L6b by one or two orders of magnitude.

In summary, the highest synaptic density was observed in L1, indicating a heightened level of connectivity and synaptic interaction. This suggests that L1 facilitates rapid information processing due to its robust synaptic activity.

Important structural subelements of SBs in the human TLN

Shape and size of PreAZs and PSDs

Synaptic efficacy, strength, modes of release and P_r are beside the pool of SVs, determined by the shape and size of AZs (Matz et al. 2010; Holderith et al. 2012; Südhof 2012).

The majority of SBs in L1 of the human TLN had a single at most three AZs that could be of the non-perforated macular or perforated type comparable with results for other layers in the human TLN (L4 Yakoubi et al. 2019b, L5: Yakoubi et al. 2019a, L6: Schmuhl-Giesen et al. 2022) but by ~1.5-fold larger than in rodent and non-human primates (Marrone et al. 2005; Rollenhagen et al. 2015, 2018; Bopp et al. 2017; Hsu et al. 2017).

The surface area of AZs in L1 SBs of the human TLN was on average ~0.20 μm^2. This is in good agreement with data obtained for AZs in L3 (Cano-Astorga et al. 2021), L4 (Yakoubi et al. 2019b), L5 (Yakoubi et al. 2019a), L6 (Schmuhl-Giesen et al. 2022) and in L3 (Cano-Astorga et al. 2023) of the human temporal and cingulate neocortex. However, they were ~2- to 3-fold larger than those in mouse and non-human primates visual, motor, and somatosensory neocortex (Bopp et al. 2017; Hsu et al. 2017) but remarkably even larger than AZs in comparably large CNS terminals like the hippocampal mossy fiber bouton (Rollenhagen et al. 2007) the cerebellar mossy fiber bouton (Xu-Frieman and Regehr 2003)and the Calyx of Held in the medial nucleus of the trapezoid body (Sätzler et al. 2002).

The substantial variability in the size of AZs at individual SBs, observed both in the human TLN and in experimental animals, likely contributes to differences in synaptic efficacy, strength, P_r, quantal size, as well as the size of the RRP and RP (Südhof 2002; Matz et al. 2010, Freche et al. 2011; Holderith et al. 2012; Neher 2015; Chamerland and Toth 2016; Rollenhagen et al. 2018; Vaden et al. 2019; reviewed by Rizzoli and Betz 2005; Denker and Rizzoli 2010). However, it has to be noted that the size of the AZ is regulated as a function of activity, as shown for hippocampal SBs in the CA1 subregion (Matz et al. 2010; Holderith et al. 2012). However, the comparably large size of the AZs in the human TLN also suggest a larger 'docking' area allowing the fusion of more SVs and thus a larger P_r.

Size of the three pools of SVs

Besides the size of the PreAZ, the pool of rapidly releasable SVs also critically determines P_r and thus synaptic efficacy, strength and plasticity (Rosenmund and Stevens 1996; Schikorski and Stevens 2001; Rizzoli and Betz 2004; Schikorski 2014; Watanabe et al. 2014; Vaden et al. 2019; reviewed by Rizzoli and

Betz 2005, Neher 2015; Chamberland and Toth 2016). It is still rather unclear whether functionally heterogeneous SV pools are structurally identifiable and thus support diverse forms of synaptic transmission und would also play a pivotal role in long- and short-term plasticity. Synaptic transmission can be modulated in various ways depending on the availability of SVs and on their recycling rates. Hence, the size of both the RRP and RP critically determines synaptic efficacy, strength and plasticity. These parameters are controlled at the PreAZ but vary substantially across various CNS synapses (reviewed by Rizzoli and Betz 2005; Neher 2015). The contribution of the RRP size to synaptic dynamics and the mechanisms by which such control is achieved at individual SBs remains largely unknown.

L1 SBs had a total pool size of ∼3500 SVs/AZ, the largest total pool size when compared with other layers of the human TLN by ~2-fold (L4, ~1800 SVs) by ~2.6-fold (L5, ~1350 SVs) and by ~3-fold (L6, ~1150 SVs), respectively. Remarkably, the total pool sizes in the human TLN were significantly larger by more than 6-fold (~550 SVs/AZ), and ~4.7-fold (~750 SVs/AZ;) than those in L4 and L5 (Yakoubi et al. 2019a, b; see also Rollenhagen et al. 2018) in rats. The largest total pool size in L1 may point to a pivotal role in the rapid replenishment after depletion by high-frequency stimulation and the transfer of SVs into the RRP and RP from the total pool in L1 SBs.

The putative RRP at L1 PreAZs was on average ~4 SVs/AZ for the p10 nm RRP and similar to that in L5 (~5 SVs/AZ), but significantly smaller by ~5.3-fold to that of L4 (~20 SVs/AZ) and by ~3.5-fold when compared to L6 in the human TLN. Also, huge differences were observed in the p20 nm RRP which at L1 PreAZs was ~20 SVs, ~40 SVs in L4, ~15 SVs in L5 and ~30 SVs in L6, respectively. It has to be noted that a layer-specific difference in both the p10 nm and p20 nm RRP exit although a huge variability was observed as indicated by the SD, IQR, and variance. Hence, at L1 PreAZs the overall RRP, taken the p10 nm and p20 nm criterion (both together are less than a vesicle diameter) was constituted by ~25 SVs rapidly available SVs that may partially contribute to the efficacy, strength and reliability of synaptic transmission, but also in the modulation of short-term synaptic plasticity in L1.

The size of the putative RP/PreAZ was ∼470 SVs in human L1 SBs and thus ~3-fold larger to that in L6 SBs, ~1.3- fold larger than in L4, and ~2.4-fold larger than in L5 SBs of the human TLN. In the rodent

neocortex the RP/PreAZ comprised ~130 (L4; see also Rollenhagen et al. 2015) and ~200 SVs (L5; see also Rollenhagen et al. 2018). The comparably largest size of the RP in L1 when compared with values for the other cortical layers in the human TLN and that found for L4 and L5 in rodents may also point to a rapid availability of SVs from the RP after the replenishment of the RRP during high-frequency stimulation. If the refilling rates were activity dependent, the large size of the RP at L1 PreAZs could explain some forms of short-term synaptic plasticity, e.g. a substantial increase in synaptic strength during frequency facilitation and post-tetanic potentiation at these SBs.

Finally, the resting pool of SVs at L1 PreAZs in the human TLN is also comparably large (~3000 SVs) and again the largest when compared with other layers in the human TLN (L4 and L5: ~1250 SVs; L6: ~900 SVs). The size of the resting pool may guarantee to rapidly replenish the RRP and RP after repetitive high-frequency stimulation via active transfer of SVs with the help of mitochondria associated with the pool of SVs (this study, see also Zhu and Fuster 1996; Verstreken et al. 2005; Smith et al. 2016).

The notable disparities in AZ and SV pool sizes among individual SBs may contribute to rapid alterations in the computational properties of single neurons or networks. Consequently, these variations in AZ and SV pool sizes at L1 SBs may critically influence the behavior of SBs during so-called Up-and-Down states as described for other SBs of the CNS (Zhou and Fuster 1996; Sanchez-Vives and McCormick 2000; Sakata and Harris 2009; Testa-Silva et al. 2014).

Importance of presynaptic mitochondria for synaptic transmission

Mitochondria in the cortical layers of the human TLN were organized in clusters associated with the pool of SVs (this study, see also Yakoubi et al. 2019a, b; Schmuhl-Giesen et al. 2022). In L1, mitochondria only contribute by about 7.2% (L1a) and 6.7% (L1b) to the total SB volume with similar values between L1 and L6, but their percentage was ~2-fold lower than values in L4 and L5 suggesting a layer-specific distribution of mitochondria in the human TLN.

Mitochondria play a role in the recruitment and mobilization of SVs from the RP and resting pool and in the priming and docking process of SVs (Verstreken et al. 2005; Perkins et al. 2010; Smith et al. 2016; reviewed by Dallerac et al. 2018). In the CNS they act as the main source of internal calcium (Pozzan and

Rizzuto 2000; Rizzuto et al. 2000), thus they regulate and control the internal calcium concentrations in CNS terminals required for the signal cascades where for example, synaptic proteins driven by Ca^{2+} like synaptotagmin, synaptophysin, synaptobrevin and the SNARE-complex are involved (Südhof 2002).

Glial coverage of L1 SBS in the human TLN

It is widely recognized that astrocytes play a crucial role in the formation of the 'tripartite' synapse, which is a common characteristic of cortical synapses. Astrocytes serve as both a physical barrier to glutamate diffusion and as mediate neurotransmitter uptake via transporters, thereby regulating the spatial and temporal concentration of neurotransmitters in the synaptic cleft (Oliet et al. 2004; Min and Nevian 2012; Pannasch et al. 2014; reviewed by Dallerac et al. 2018). In addition, they modulate synaptic transmission by activating pre- and postsynaptic receptors (Haydon and Carmignoto 2006; Le Meur et al. 2012). Moreover, it was found that the control of t-LTD at neocortical synapses is critically influenced by astrocytes by increasing Ca^{2+} signaling during the induction of t-LTD (Min and Nevian 2012).

Remarkably, significant layer-specific differences exist in the astrocytic coverage of synaptic complexes in the human TLN. Whereas in L4 and L5 ~80% of the total volumetric fraction was occupied by astrocytic processes and most of synaptic complexes were tightly ensheathed by fine astrocytic processes, in L1 and L6 the volumetric fraction of astrocytic processes was only ~30% with a loose and incomplete coverage of synaptic complexes. As a consequence, the lack or incomplete astrocytic coverage of synaptic complexes in L1 can only partially act as a physical barrier to neurotransmitter diffusion. In addition, beside a vertical also its horizontal diffusion of glutamate at the synaptic cleft is possible. Hence, two possible scenarios for the role of astrocytes are present at L1 synaptic complexes. First, as shown for only a small part of synaptic complexes in L1 the 'tripartite' synapse is realized at both sides of the synaptic cleft. This would allow the selective uptake of horizontally diffusing glutamate via glutamate transporters located in the fine astrocytic processes. This prevents 'glutamate spillover', and thus allow a vertically directed neurotransmitter diffusion and docking to postsynaptic receptors at the PSD.

The remaining larger part of synaptic complexes in L1 either lack a coverage by fine astrocytic processes or are only partially ensheathed. Here 'glutamate spillover' of horizontally diffusing neurotransmitter quanta is most likely and thus synaptic crosstalk between neighboring synaptic complexes at AZs in neighboring spines on terminal tuft dendrites because spine density in L1 is high. This may cause a switch from asynchronous to synchronous release from neighboring synaptic complexes upon repetitive low- and high-frequency stimulation (von Gersdorff and Borst 2002).

In summary, two distinct structural scenarios were identified regarding the role of astrocytes in L1, However, it is still rather unknown which of the two scenarios contribute more efficiently to synaptic transmission and plasticity in L1.

The role of L1 in the information processing of the cortical column

The computational properties of the neocortex depend upon its ability to integrate the information provided by the sensory organs (bottom-up information) with internally generated signals such as expectations or attentional signals (top-down information). This integration occurs in apical tuft dendrites in L1. Importantly, L1 is the predominant input layer for top-down information, relayed by a rich, dense network of cortico-cortical, commissural and associational long-range axonal projections and L1 excitatory and inhibitory neurons providing signals to the terminal tuft dendrites of pyramidal neurons (reviewed by Schumann et al. 2021). Thus, L1 is a central locus of neocortical associations controlled by distinct types of excitation and inhibition in humans (reviewed by Hartung and Letzkus 2021).

From L4, as the first station of intracortical information processing thalamocortical signals are transferred via intracolumnar projecting axonal collaterals via L2, L3 to L1 (Feldmeyer et al. 1999; Lübke et al. 2000) representing a convergent input layer for thalamocortical and cortico-cortical synaptic inputs. Hence, L4 excitatory neurons act as 'feed-back amplifiers', but also guarantee a highly reliable signal transduction to L2, L3 and L1 (Feldmeyer et al. 1999; Seeman et al. 2018).

SBs in L1 may contact both the persistent population of CR-cells, GABAergic interneurons and terminal tuft dendrites of pyramidal neurons (Figure 7) proving feed-forward excitation to their putative partners in

L1. CR-cells exhibit long-range excitation within and across cortical columns via long horizontal axonal collaterals that preferentially and heavily contact terminal tuft dendrites of pyramidal neurons (Anstötz et al. 2014). As shown in rodent neocortex, GABAergic interneurons are synaptically coupled with CR-cells providing feed-forward inhibition (Anstötz et al. 2014). Another subpopulation of GABAergic interneurons in L1 provide a highly specialized form of recurrent inhibition that link cortical L1 to L3 interneurons and L5 pyramidal neurons (Jiang et al. 2013). L1 single-bouquet cells preferentially form inhibitory connections on L2/3 interneurons that inhibit the entire dendritic-somato-axonal axis of L5 pyramidal neurons located within the same column. In contrast, L1 neurogliaform cells frequently form inhibitory and electric connections with L2/3 interneurons. These L1-L3 interneurons inhibit the distal apical dendrite of > 60% of L5 pyramidal neurons across multiple columns. Functionally, the single bouquet cell to L2/3 interneurons to L5 pyramidal neuronal circuits disinhibit, and neurogliaform cells to L2/3 interneuron to L5 pyramidal neuronal circuits inhibit the initiation of dendritic complex spikes in L5 pyramidal neurons. As dendritic complex spikes can serve coincidence detection, these cortical interneuronal circuits may be essential for salience selection (Jiang et al. 2013).

Finally, L1 receive GABAergic input from Martinotti cells located in L2/3 and L5, axo-axonic Chandelier cells in L2/3 and VIP-expressing interneurons in L2 all of which have a very prominent axonal plexus in L1 (Figure 7, see also Silberberg and Markram 2007; Obermayer et al. 2018; reviewed by Hartung and Letzkus 2021; Schuman et al. 2021).

In summary, these interneuron populations provide inhibition and disinhibition to pyramidal terminal tuft dendrites by either shunting or promoting the generation of Ca^{2+}- and Na^{+}-spikes by temporal and spatial coincidence detection. Thus, the circuitry of L1 is an important and fundamental ‘integrator’ of the neocortex sampling bottom-up information within or even across cortical columns, but also act as a ‘filter’ or ‘discriminator’ but also as an ‘amplifier’ in the information processing of the neocortex.

Hence, L1 of the neocortex can be regarded as a complex and intricate layer of the brain serving different functions, for example to gate inputs, convey expectations and context as well as mediate states of consciousness, attention, cross-modal interactions, sensory perception, and learning (Bastos et al. 2012;

Heeger 2017; Zagha 2020; reviewed by Gilbert and Li 2013). There is evidence that L1 processing, particularly Ca^{2+} signals in the distal apical dendrite, is important for sensory perception (Xu et al. 2012). Recent studies have revealed that L1 plays a crucial role in top-down attentional processes, aiding in directing attention, based on our goals and intentions (Hartung and Letzkus 2021; Schuman et al. 2021). Additionally, L1 is implicated in the formation and consolidation of long-term memories with disruptions in L1 function associated with memory deficits. Furthermore, L1 contributes to brain plasticity, which involves the brain's ability to change and adapt in response to experience, including the process by which synapses alter in strength and number (reviewed by Hartung and Letzkus 2021; Schuman et al. 2021).

Overall, L1 of the neocortex is a complex and fascinating layer of the brain that is involved in a wide range of cognitive processes and brain plasticity. Since this is relayed by a network of SBs in L1, their composition and connections play a pivotal role, in columnar information processing.

Material and Methods

Human brain tissue sampling during epilepsy surgery have been provided by Dr. med. Dorothea Miller, PD Dr. med. Marec von Lehe, Department of Neurosurgery, Knappschaftschafts/Universitäts-Krankenhaus Bochum and were approved by the Ethical Committees of the Rheinische Friedrich-Wilhelms-University/University Hospital Bonn (Ethical votum of the Medical Faculty to Prof. Dr. med. Johannes Schramm and Prof. Dr. rer. nat. Joachim Lübke, Nr. 146/11), the University of Bochum (Ethical votum of the Medical Faculty to PD Dr. med. Marec von Lehe and Prof. Dr. rer. nat. Joachim Lübke, Reg. No. 5190-14-15; and renewed Ethical votum of the Medical Faculty to Dr. med. Dorothea Miller and Prof. Dr. rer. nat. Joachim Lübke, Reg. No. 17–6199-BR). The consent of the patients was obtained by written and signed statements, and all further experimental procedures were approved by the same Ethical Committees cited above, and the EU directive (2015/565/EC and 2015/566/EC) concerning working with human tissue used for experimental and scientific purposes.

All subsequent experimental procedures were approved by the Research Committee of the Research Centre Jülich GmbH.

Fixation and tissue processing for TEM

Tissue samples from the human TLN were after their removal prepared and embedded for conventional TEM and EM tomography analysis. All neocortical access tissues were obtained from patients (1 male and 3 female, 24-65 years in age, see Supplemental Table 1) suffering from drug-resistant temporal lobe epilepsy. The pre-surgical work-up comprised at least high-resolution magnetic resonance imaging together with long-term video-electro-encephalography (EEG)-monitoring. In all cases, the circumscribed epileptic focus was in the hippocampus proper, but not in the neocortical access regions of the TL.

During epilepsy surgery, blocks of both non-affected, non-epileptic and epileptic neocortical access tissue samples (see Supplemental Table 1) were resected to control the seizures for histological inspection by neuropathologists. The non-affected non-epileptic neocortical access tissue samples was always taken far from the epileptic focus and may thus be regarded as non-epileptic as also demonstrated by other structural and functional studies using the same experimental approach (Alonso-Nanclares 2008; Navarette et al. 2013; Mohan et al. 2015; Molnár et al. 2016, Seeman et al. 2018; reviewed by Mansfelder et al. 2019). So-called 'post mortem' tissue was not used in this study since the ultrastructural quality (preservation) of such material is not suitable enough for fine-scale high-resolution EM, due to severe distortions of relevant structural features, e.g. fragmentation and lysis of membranes of SBs, PreAZs, PSDs and SVs that are required for the generation of quantitative 3D-models of SBs and their target structures (Lübke, personal observation). However, under certain conditions also 'post mortem' tissue samples can be used (Dominguez-Alvaro et al. 2019, 2921; Cano-Astorga et al. 2021, 2023).

Inter-individual differences were found in the structural and synaptic parameters analyzed as shown by the box plots (Supplemental Figures 1, 2; Source Data 2).

Other recent studies using the same experimental approach neglected and thus discarded the effect of the pharmacological treatments and disease condition (Alonso-Nanclares et al. 2008; Testa Silva et al. 2014; Mohan et al. 2015; Molnár et al. 2016; Seeman et al. 2018; Dominguez-Alvaro et al. 2019; Yakoubi et al. 2019a, b; Schmuhl-Giesen et al. 2022).

For the study of L1 in the human TLN, blocks of neocortical access tissue were sampled from the temporo-lateral or temporo-basal regions of the inferior temporal gyrus and the gyrus medialis. Immediately after their removal

during epilepsy surgery, biopsy samples of the TLN were immersion-fixed in ice-cold 4% paraformaldehyde and 2.5% glutaraldehyde diluted in 0.1 M phosphate buffer (PB, pH 7.4) for 24-72 hrs at 4°C. The fixative was replaced by fresh fixative after 2 hrs and changed twice during the subsequent fixation period. Prior to vibratome sectioning, brain tissue samples were thoroughly rinsed in ice-cold PB and afterwards embedded in 5% Agar-Agar (Sigma, Munich, Germany) diluted in PB.

Neocortical tissue blocks were cut in the coronal plane through the TLN with a Vibratome VT 1000S (Leica Microsystems GmbH, Wetzlar, Germany) into 150-200 µm thick sections, collected in ice-cold PB, and washed again several times in PB. Afterwards they were transferred to 0.5-1% PB-sucrose buffered Osmium tetroxide (OsO_4, 300 mOsm, pH 7.4; Sigma, Munich, Germany) for 60-90 min. After visual inspection to check for the quality of post-fixation, sections were thoroughly washed several times in PB and left overnight at 4°C in PB. The next day they were dehydrated in an ascending series of ethanol starting at 20%, 30%, 50%, 60%, 70%, 80%, 90%, 95% to absolute ethanol (15 min for each step and absolute ethanol, 30 min twice), followed by a brief incubation in propylene oxide (2 min twice; Fluka, Neu-Ulm, Germany). Sections were then transferred into a mixture of propylene oxide and Durcupan™ resin (2:1, 1:1 for 1h each; Fluka, Neu-Ulm, Germany) and stored overnight in pure resin. The next day, sections were flat embedded on coated glass slides in fresh Durcupan™, coverslipped with Acla™ foils and polymerized at 60°C for 2 days.

Semi- and ultrathin sectioning

After light microscopic (LM) inspection, a tissue block containing the region of interest (ROI) was glued on a pre-polymerized block and trimmed down. Semithin sections were cut with a Leica UltracutS ultramicrotome (Leica Microsystems, Vienna, Austria), with a Histo-Diamond knife (Fa. Diatome, Nidau, Switzerland). Afterwards they were briefly stained with methylene-blue (Sigma-Aldrich Chemie GmbH, Taufkirchen, Germany) to identify the cortical layers, particularly L1 and underlying L2, examined and documented using a motorized Olympus BX61 microscope equipped with the Olympus CellSense analysis hard- and software (Olympus GmbH, Hamburg, Germany). All images were stored in a database until further use.

After further trimming of the block to its final size, serial ultrathin sections (50 ± 5 nm thickness; silver to silver gray interference contrast) were cut with a Leica UltracutS ultramicrotome through the determined ROI of L1a and L1b, respectively. Ultrathin sections in serial sequence were collected on pioloform-coated slot copper grids (Plano, Wetzlar, Germany). Prior to EM examination, sections were stained with 5% aqueous uranyl acetate or Uranyless (Science Services, Munich, Germany) for 15–20 min and lead citrate for 3–5 min according to Reynolds (1963) to enhance the contrast of biological membranes at the EM level. In each series of ultrathin sections, two or three ROIs throughout L1a or L1b were chosen, and photographed at a final EM magnification of 8000x with a Zeiss Libra 120 (Fa. Zeiss, Oberkochen, Germany) equipped with a Proscan 2K digital camera (Fa. Tröndle, Moorenweis, Germany) using the ImageSP software and its panorama function (Fa. Tröndle, Moorenweis, Germany). In addition, interesting details of synaptic structures in L1a and L1b were taken at various EM magnifications.

All images were stored in a database until further use. Selected EM images for publication were further edited using Adobe Photoshop™ and Adobe Illustrator™ software.

3D-volume reconstructions and quantitative analysis of SBs

EM panorama images composing each series were imported, stacked, and aligned in the reconstruction software OpenCAR (Contour Alignment Reconstruction; for details see Sätzler et al. 2002). The main goal of this study was to quantify several structural and synaptic parameters representing structural correlates of synaptic transmission and plasticity. Excitatory SBs were characterized by large round SVs and prominent PreAZs and PSDs in contrast to putative GABAergic terminals that have smaller, more oval-shaped SVs, and a thin or no PSDs.

The following structural parameters were analyzed: (1) surface area and volume of SBs; (2) volume of mitochondria; (3) surface area of PreAZs (Dufour et al. 2016) and PSDs; two apposed membrane specializations separated by the synaptic cleft; (4) number and diameter of clear SVs and dense-core vesicles (DCVs); and (5) distance of individual SVs from the PreAZ for the structural definition of the RRP, RP, and resting pool. 3D-volume reconstructions were generated by drawing contour lines on the structures of interest in each panorama image within a series of images until a given structure was completed. Presynaptic SBs, their mitochondria as well as their postsynaptic target structures were outlined on the outer edge of their membranes, using closed contour lines

throughout the entire stack within a series. A SB was considered completely captured, when it was possible to follow the axon in both directions through the entire series (*en passant* SBs) or the enlargement of the axon leading to an endterminal SB. The beginning of a synaptic terminal was defined by the typical widening of the axon and the abrupt occurrence of a pool of SVs.

The PreAZs and PSDs were regarded as complete when their perimeters were entirely reconstructed in a series of ultrathin sections. The surface areas of the PreAZ and PSD were computed separately by first generating a 3D surface model of the SB. The PreAZ was then measured by extracting this area from the reconstructed presynaptic bouton membrane that was covered by this membrane specialization. Hence, the length (L) of the PreAZ (L PreAZ) and the surface area (SA) of the PreAZ (SA PreAZ) is already known.

The size of the PSD opposing the PreAZ was estimated under the following assumptions: (1) both membrane specializations, PreAZ and PSD run parallel to each other at the pre- and postsynaptic apposition zone; (2) for both membrane specializations a contour line was drawn determining their actual length (L PreAZ and L PSD). Hence, the surface area of the PSD (SA PSD) is estimated by the following equation:

$$\mathbf{SA\ PSD = SA\ PreAZ * L\ PSD/L\ PreAZ}$$

which is the perimeter ratio between the outlines of the PSD to that of the synaptic contact.

The synaptic cleft width was measured because of its importance for the transient temporal and spatial increase of the glutamate concentration, reversible binding of glutamate to appropriate glutamate receptors and eventual up-take and diffusion of glutamate out of the synaptic cleft. To a large extent, these processes are governed by the geometry of this structure and the shape and size of the PreAZs and PSDs.

Measurements of the width of the synaptic cleft were performed on random EM images taken from the series using OpenCAR or online directly at the EM using ImageSP (Fa. Tröndle, Moorenweis, Germany). Only synaptic clefts cut perpendicular to the PreAZ and PSD were included in the sample. The distance between the outer edge of the pre- and postsynaptic membranes was measured at the two lateral edges and separately at the central region of the synaptic cleft; the two values of the lateral edges were averaged for each cleft measurement. Finally, a mean ± SD was calculated for both the lateral and central region over all synaptic clefts analyzed per patient.

All SVs were marked throughout each SB, their diameters were individually measured and their distances to the PreAZ were automatically detected using an algorithm implemented in OpenCAR (minimal distance between each SV membrane to the contour line of the PreAZ) throughout the SB in every single image of the series. Large DCVs were only counted in the image where they appeared largest. To avoid double counts, only clear ring-like structures were counted as SVs. However, SVs might be missed in densely packed regions, because ring-like traces may partly overlap. This effect may counteract any double counts. Based on the small extent and the partially counteracting nature of this effect, the numbers of small clear vesicles reported in this study remained uncorrected (Yakoubi et al. 2019a, b, Schmuhl-Giesen et al. 2022).

In this work, aldehyde fixation was used that is thought to induce tissue shrinkage thereby biasing structural quantification (Eyre et al. 2007; Korogod et al. 2015). A direct comparison of structural parameters obtained from either aldehyde or cryo-fixed and substituted tissue samples (Korogod et al. 2015), showed differences in cortical thickness (~16% larger in cryo-fixed material), in the volume of extracellular space (~6-fold larger in cryo-fixed material), a slight increase in glial volume and overall density of synaptic contacts (~14% in cryo-fixed material), but no significant differences in neuronal structures such as axons, dendrites and SV diameter.

In the structural and synaptic parameters as estimated here, no significant difference was found for SB size and other synaptic subelements such as mitochondria, active zones (AZs) and SVs when compared with other studies (Zhao et al. 2012a, b). Therefore, no corrections for shrinkage were applied and we are thus convinced that the synaptic parameters reported here are accurate and can be directly used for detailed computational models. In addition, large-scale preservation for ultrastructural analysis will therefore continue to rely on chemical fixation approaches, due to the limited preservation of the ultrastructure in cryo-fixed material as stated in Korogod and co-workers (2015).

Golgi-Cox impregnation of biopsy material in L4 of the human TLN

To get an impression about the neuronal organization of the human TLN, four tissue blocks were processed with the Golgi-Cox impregnation technique using the commercially available Hito Golgi-Cox OptimStain kit (Hitobiotec Corp, Kingsport, TE, USA). After removal of the biopsy samples, tissues were briefly rinsed twice in double distilled

water (dd H_2O), and then transferred into impregnation solution 1 overnight at room temperature. The next day, tissue samples were incubated in fresh impregnation solution 1 and stored for 14 days in the dark at room temperature. Sections were then transferred in solution 3 and kept in the dark at room temperature for one day. Thereafter, sections were placed into fresh solution 3 in the dark at room temperature for 6 additional days. Then, solution 3 was exchanged and samples were stored at 4°C in the dark overnight. Tissue blocks were embedded in 5% agarose (Carl Roth, Karlsruhe, Germany) diluted in ddH_2O, and sectioned with a vibratome in the coronal plane at 100–250 µm thickness and then transferred to ddH_2O.

After careful removal of the agarose, free-floating sections were incubated into solution 3 for 2–3 min in the dark at room temperature, and right after placed into ddH_2O, washed several times and stored overnight. Afterwards, they were rinsed twice in ddH_2O for 4 min each, and dehydrated in 50%, 70% and 95% ethanol for 5 min each, then transferred into absolute ethanol (3 × 5 min), defatted in xylene, embedded in Eukitt™ (Sigma-Aldrich Chemie GmbH, Taufkirchen, Germany), finally coverslipped and air-dried. Afterwards, sections were examined and imaged with an Olympus BX 61 LM equipped with the CellSense software package (Olympus, Hamburg, Germany) at various magnifications and images were stored in a database until further use.

Stereological estimation of the density of L1 synaptic contacts in the human TLN

The density of synaptic complexes, composed either between an SB with a dendrite or spine, in a given volume is a valuable parameter to assess the structural and functional changes in the brain, which are linked to the age, pathological or experimental conditions (Rakic et al. 1994; DeFelipe et al. 1999). The density of synaptic contacts was unbiasedly estimated in L1, separated for L1a and L1b, from four patients, respectively (Supplemental Table 1; Source Data 1) using the physical dissector technique (Mayhew 1996; Fiala and Harris 2001) by counting the synaptic complexes in a virtual volume generated by two adjacent ultrathin sections that is the dissector: the reference section and the look-up section. Here, counting was performed using FIJI (Schindelin et al. 2012) on a stack of 20 aligned serial electron micrographs for each patient taken from the series of ultrathin sections used for the 3D-volume reconstructions of SBs in L1. An unbiased counting frame was first set and synaptic contacts to be considered (counted) are the one present in the reference section only and meeting the following criteria: presence

of a PreAZ and a prominent or thin PSD separated by a synaptic cleft and SVs in the presynaptic terminal. Care was taken to distinguish between excitatory and inhibitory synaptic contacts, as well as the postsynaptic target structures (dendritic shafts or spines). Finally, the density of synaptic contacts (*Nv*) per 1 mm^3 was calculated using the formula below:

$$\mathbf{Nv=\sum Qd/\sum Vd}$$

where *Qd* is the number of synaptic contacts per dissector and Vd is the volume of the dissector given by: Number of dissectors x frame area x section thickness.

EM tomography of L1 SBs in the human TLN

EM tomography was performed on 200-300 nm thick sections cut from blocks prepared for serial ultrathin sectioning as described above (Table 2; Source Data 3). Sections were mounted on pioloform-coated line copper grids and were counterstained with uranyl acetate and lead citrate following a slightly modified staining protocol as described by Reynolds (1063).

Subsequently, sections were examined with a JEOL JEM 1400Plus, operating at 120 kV and equipped with a 4096×4096 pixels CMOS camera (TemCam-F416, TVIPS, Gauting, Germany). Tilt-series were acquired automatically over an angular range of −60° to +60° at 1°-degree increments using Serial EM (Mastronarde 2005). Stack alignment and reconstruction by filtered backprojection were carried out using the software package iMOD (Kremer et al. 1963). Final reconstructions were ultimately filtered using a median filter with a window size of 3 pixels. Tilt-series were stored as .tif files and were further processed using the freely available software Imod 4.9.12 and ImageJ (ImageJ, RRID:SCR-0033070). In each tilt-series so-called 'docked' SVs identified by their fusion with the PreAZ or as omega-shaped body that already released a quantum of neurotransmitter were counted separately for L1a and L1b and for their target structures, dendritic shafts or spines.

Quantitative analysis of the astrocytic coverage

To quantify the astrocytic coverage of synaptic complexes that may or may not constitute the 'tripartite' synapse in the human neocortex, the interactive software ImageJ (Schneider et al. 2012) was used. The first, the middle, and

the last images of an individual EM series were used for a further quantitative volumetric analysis (Source Data 4). In each section of the same series used for the 3D-volume reconstructions, a grid (grid size 1 × 1 μm^2) was placed over the EM image, and in each square, the abundance of fine astrocytic processes was documented throughout these images and averaged. Using the Cavalieri method [Unbiased Stereology: Three-Dimensional Measurement in Microscopy (Advanced Methods) Paperback-January 7, 2005, by Vyvyan Howard Matthew Reed], the (absolute) volume contribution of astrocytic processes was determined according to the Cavalieri estimator:

$$\mathbf{V=a(p)\times\Sigma P\times t}$$

where a(p) is the size of one square (0.8 × 0.8 μm2), P is the number of squares counted, and t is the thickness of the slice.

Statistical analysis

The mean value ± standard deviation (SD), the median with the interquartile range (IQR), the coefficient of variation (CV), skewness, variance, and the coefficient of correlation (R^2) were given for each structural parameter analyzed. The p-value was considered significant only if $p < 0.05$. Box- and Violin plots (Plotly 4.0.0 https://chart-studio.plotly.com) were generated to investigate inter-individual differences for each patient and structural parameter (Supplemental Figure 1, 2; Source Data 2).

To test for significant differences between L1a and L1b, the non-parametric Kruskal-Wallis H-test with a subsequent Mann-Whitney u-test analysis was performed, using PAST 4.02 (Hammer et al. 2001). Correlation graphs between several structural parameters were then generated (Figure 4). The R^2-values were interpreted as follows: 0, no linear correlation; 0-0.5, weak linear correlation; 0.5-0.8, good linear correlation; and 0.8-1.0, strong linear correlation. Furthermore, a freely available Fisher's *r*-to-*z*-transformation calculator (Fisher's z) was used to test for differences in R^2 between L1a and L1b (p-value < 0.05).

Acknowledgments

We would like to thank our technicians Brigitte Marshallsay and Tayfun Palaz for their excellent technical assistance. Furthermore, the constant financial support of the Helmholtz Society is very much acknowledged.

References

Allone, C., Lo Buono, V., Corallo, F., Pisani, L.R., Pollicino, P., Bramanti, P., and Marino, S. (2017). Neuroimaging and cognitive functions in temporal lobe epilepsy: A review of the literature. J. Neurol. Sci. 381, 7-15. 10.1016/j.jns.2017.08.007.

Alonso-Nanclares, L., Gonzalez-Soriano, J., Rodriguez, J.R., and DeFelipe, J. (2008). Gender differences in human cortical synaptic density. Proc. Natl. Acad Sci. USA 105, 14615-14619. 10.1073/pnas.0803652105.

Anstötz, M., Cosgrove, K.E., Hack, I., Mugnaini, E., Maccaferri, G., Lübke, J.H.R. (2014), Morphology, input-output relations and synaptic connectivity of Cajal-Retzius cells in layer 1 of the developing neocortex of CXCR4-EGFP mice. Brain Struct Funct 219, 2119-2139. 10.1007/s00429-013-0627-2.

Bastos, A.M., Usrey, W.M., Adams, R.A., Mangun, G.R., Fries, P., and Friston, K.J. (2012). Canonical microcircuits for predictive coding. Neuron 76, 695-711. 10.1016/j.neuron.2012.10.038.

Blazquez-Llorca, L., Merchan-Perez, A., Rodriguez, J.R., Gascon, J., and DeFelipe, J. (2013). FIB/SEM technology and Alzheimer's disease: three-dimensional analysis of human cortical synapses. J. Alzheimers Dis. 34, 995-1013. 10.3233/JAD-122038.

Bopp, R., Holler-Rickauer, S., Martin, K.A.C., and Schuhknecht, G.F. (2017). An Ultrastructural Study of the Thalamic Input to Layer 4 of Primary Motor and Primary Somatosensory Cortex in the Mouse. J. Neurosci. 37, 2435-2448. 10.1523/JNEUROSCI.2557-16.2017.

Bystron, I., Blakemore, C., and Rakic, P. (2008). Development of the human cerebral cortex: Boulder Committee revisited. Nat. Rev. Neurosci. 9, 110-122. 10.1038/nrn2252.

Cajal, S.R. (1911). Histology of the nervous system of man and vertebrates. History of Neuroscience (Oxford Univ Press, New York, 1995).

Cano-Astorga, N., DeFelipe, J., and Alonso-Nanclares, L. (2021). Three-Dimensional Synaptic Organization of Layer III of the Human Temporal Neocortex. Cereb. Cortex 31, 4742-4764. 10.1093/cercor/bhab120.

Cano-Astorga N, Plaza-Alonso S, DeFelipe J, Alonso-Nanclares L (2023), 3D synaptic organization of layer III of the human anterior cingulate and temporopolar cortex. Cereb. Cortex 33, 9691-9708. 10.1093/cercor/bhad232.

Chamberland, S., and Toth, K. (2016). Functionally heterogeneous synaptic vesicle pools support diverse synaptic signalling. J. Physiol. 594, 825-835. 10.1113/JP270194.

Cooper, J.A. (2008). A mechanism for inside-out lamination in the neocortex. Trends Neurosci. 31, 113-119. 10.1016/j.tins.2007.12.003

Dallerac, G., Zapata, J., and Rouach, N. (2018). Versatile control of synaptic circuits by astrocytes: where, when and how? Nat. Rev. Neurosci. 19, 729-743. 10.1038/s41583-018-0080-6.

DeFelipe, J., Marco, P., Busturia, I., and Merchan-Perez, A. (1999). Estimation of the number of synapses in the cerebral cortex: methodological considerations. Cereb. Cortex 9, 722-732. 10.1093/cercor/9.7.722.

DeFelipe, J., Oroquieta, J., Arellano, J.I., Alonso, L., and Munoz, A. (2002). The neuropathology of temporal lobe epilepsy: primary and secondary changes in the cortical circuits and epileptogenicity. Rev. Neurol. 34, 401-408.

Deller, T., Korte, M., Chabanis, S., Drakew, A., Schwegler, H., Stefani, G.G., Zuniga, A., Schwarz, K., Bonhoeffer, T., Zeller, R., et al. (2003). Synaptopodin-deficient mice lack a spine apparatus and show deficits in synaptic plasticity. Proc. Natl. Acad. Sci. USA 100, 10494-10499. 10.1073/pnas.1832384100.

Denker, A., and Rizzoli, S.O. (2010). Synaptic vesicle pools: an update. Front. Synaptic. Neurosci. 2, 135. 10.3389/fnsyn.2010.00135.

Dufour, A., Rollenhagen, A., Sätzler, K., and Lübke, J.H.R. (2016). Development of Synaptic Boutons in Layer 4 of the Barrel Field of the Rat Somatosensory Cortex: A Quantitative Analysis. Cereb. Cortex 26, 838-854. 10.1093/cercor/bhv270.

Dominguez-Alvaro, M., Montero-Crespo, M., Blazquez-Llorca, L., DeFelipe, J., and Alonso-Nanclares, L. (2019). 3D Electron Microscopy Study of Synaptic Organization of the Normal Human Transentorhinal Cortex and Its Possible Alterations in Alzheimer's Disease. eNeuro 6. 10.1523/ENEURO.0140-19.2019

Dominguez-Alvaro, M., Montero-Crespo, M., Blazquez-Llorca, L., DeFelipe, J., and Alonso-Nanclares, L. (2021). 3D Ultrastructural Study of Synapses in the Human Entorhinal Cortex. Cereb. Cortex 31, 410-425. 10.1093/cercor/bhaa233.

Economo, C. F. von and Koskinas, G. N. (1925) Die Cytoarchitektonik der Hirnrinde des erwachsenen Menschen, J. Springer, Berlin und Wien. 10.1007/978-3-642-37824-9

Eyre, M.D., Freund, T.F., and Gulyas, A.I. (2007). Quantitative ultrastructural differences between local and medial septal GABAergic axon terminals in the rat hippocampus. Neuroscience 149, 537-548. 10.1016/j.neuroscience.2007.08.006

Feldmeyer, D., Egger, V., Lübke, J., and Sakmann, B. (1999). Reliable synaptic connections between pairs of excitatory layer 4 neurones within a single 'barrel' of developing rat somatosensory cortex. J. Physiol. 521, 169-190. 10.1111/j.1469-7793.1999.00169.x.

Fiala, J.C., and Harris, K.M. (2001). Extending unbiased stereology of brain ultrastructure to three-dimensional volumes. J. Am. Med. Inform. Assoc. 8, 1-16. 10.1136/jamia.2001.0080001.

Finnema, S.J., Nabulsi, N.B., Eid, T., Detyniecki, K., Lin, S.F., Chen, M.K., Dhaher, R., Matuskey, D., Baum, E., Holden, D., et al. (2016). Imaging synaptic density in the living human brain. Sci. Transl. Med. 8, 348-396. 10.1126/scitranslmed.aaf66.

Freche, D., Pannasch, U., Rouach, N., and Holcman, D. (2011). Synapse geometry and receptor dynamics modulate synaptic strength. PLoS One *6*, e25122. 10.1371/journal.pone.0025122.

Ghijsen, W.E., and Leenders, A.G. (2005). Differential signaling in presynaptic neurotransmitter release. Cell. Mol. Life Sci. 62, 937-954. 10.1007/s00018-004-4525-0.

Gilbert, C.D., and Li, W. (2013). Top-down influences on visual processing. Nat. Rev. Neurosci. 14, 350-363. 10.1038/nrn3476.

Hartung, J., and Letzkus, J.J. (2021). Inhibitory plasticity in layer 1 - dynamic gatekeeper of neocortical associations. Curr. Opin. Neurobiol. 67, 26-33. 10.1016/j.conb.2020.06.003.

Hammer, Ø., Harper, A.T., and Ryan P.D. (2001). Past: paleontological statistics software package for education and data analysis. Palaeontologia Electronica. 4, 1–9; https://palaeo-electronica.org/2001_1/past/issue1_01.htm.

Haydon, P.G., and Carmignoto, G. (2006). Astrocyte control of synaptic transmission and neurovascular coupling. Physiol. Rev. 86, 1009-1031. 10.1152/physrev.00049.2005.

Heeger, D.J. (2017). Theory of cortical function. Proc. Natl. Acad. Sci. USA 114, 1773-1782. 10.1073/pnas.1619788114.

Hsu, A., Luebke, J.I., and Medalla, M. (2017). Comparative ultrastructural features of excitatory synapses in the visual and frontal cortices of the adult mouse and monkey. J. Comp. Neurol. 525, 2175-2191. 10.1002/cne.24196.

Holderith, N., Lorincz, A., Katona, G., Rozsa, B., Kulik, A., Watanabe, M., and Nusser, Z. (2012). Release probability of hippocampal glutamatergic terminals scales with the size of the active zone. Nat. Neurosci. 15, 988-997. 10.1038/nn.3137.

Insausti, R. (2013). Comparative neuroanatomical parcellation of the human and nonhuman primate temporal pole. J. Comp. Neurol. 521, 4163-4176. 10.1002/cne.23431.

Jiang, X., Wang, G., Lee, A.J., Stornetta, R.L., and Zhu, J.J. (2013). The organization of two new cortical interneuronal circuits. Nat. Neurosci. 16, 210-218. 10.1038/nn.3305.

Kiernan, J.A. (2012). Anatomy of the temporal lobe. Epilepsy Res. Treat 2012, 176157. 10.1155/2012/176157.

Knott, G., and Holtmaat, A. (2008). Dendritic spine plasticity--current understanding from in vivo studies. Brain Res. Rev. 58, 282-289. 10.1016/j.brainresrev.2008.01.002.

Korogod, N., Petersen, C.C., and Knott, G.W. (2015). Ultrastructural analysis of adult mouse neocortex comparing aldehyde perfusion with cryo fixation. Elife 4. 10.7554/eLife.05793

Kremer, J.R., Mastronarde, D.N., and McIntosh, J.R. (1996). Computer visualization of three-dimensional image data using IMOD. J. Struct. Biol. 116, 71-76. 10.1006/jsbi.1996.0013.

Krencik, R., van Asperen, J.V., and Ullian, E.M. (2017). Human astrocytes are distinct contributors to the complexity of synaptic function. Brain Res. Bull. 129, 66-73. 10.1016/j.brainresbull.2016.08.012.

Le Meur, K., Mendizabal-Zubiaga, J., Grandes, P., and Audinat, E. (2012). GABA release by hippocampal astrocytes. Front. Comput. Neurosci. 6, 59. 10.3389/fncom.2012.00059.

Luskin, M.B., and Shatz, C.J. (1985a). Neurogenesis of the cat's primary visual cortex. J. Comp. Neurol. 242, 611-631. 10.1002/cne.902420409.

Luskin, M.B., and Shatz, C.J. (1985b). Studies of the earliest generated cells of the cat's visual cortex: cogeneration of subplate and marginal zones. J. Neurosci. 5, 1062-1075. 10.1523/JNEUROSCI.05-04-01062.1985.

Lübke, J., Egger, V., Sakmann, B., and Feldmeyer, D. (2000). Columnar organization of dendrites and axons of single and synaptically coupled excitatory spiny neurons in layer 4 of the rat barrel cortex. J. Neurosci. 20, 5300-5311. 10.1523/JNEUROSCI.20-14-05300.2000.

Lübke, J., and Feldmeyer D (2007). Excitatory signal flow and connectivity in a cortical column: focus on barrel cortex. Brain Struct Funct 212, 3-17. 10.1007/s00429-007-0144-2.

Mansvelder, H.D., Verhoog, M.B., and Goriounova, N.A. (2019). Synaptic plasticity in human cortical circuits: cellular mechanisms of learning and memory in the human brain? Curr. Opin. Neurobiol. 54, 186-193. 10.1016/j.conb.2018.06.013.

Marin-Padilla, M. (1978). Dual origin of the mammalian neocortex and evolution of the cortical plate. Anat. Embryol. (Berl) 152, 109-126. 10.1007/BF00315920.

Marco, P., and DeFelipe, J. (1997). Altered synaptic circuitry in the human temporal neocortex removed from epileptic patients. Exp. Brain Res. 114, 1-10. 10.1007/pl00005608.

Marrone, D.F., LeBoutillier, J.C., and Petit, T.L. (2005). Ultrastructural correlates of vesicular docking in the rat dentate gyrus. Neurosci. Lett. 378, 92-97. 10.1016/j.neulet.2004.12.019.

Matz, J., Gilyan, A., Kolar, A., McCarvill, T., and Krueger, S.R. (2010). Rapid structural alterations of the active zone lead to sustained changes in neurotransmitter release. Proc. Natl. Acad. Sci. USA 107, 8836-8841. 10.1073/pnas.0906087107.

Mayhew, T.M. (1996). How to count synapses unbiasedly and efficiently at the ultrastructural level: proposal for a standard sampling and counting protocol. J. Neurocytol. 25, 793-804. 10.1007/BF02284842.

Marin-Padilla, M. (1998). Cajal-Retzius cells and the development of the neocortex. Trends Neurosci. 21, 64-71. 10.1016/s0090-4295(98)00190-3.

Min, R., and Nevian, T. (2012). Astrocyte signaling controls spike timing-dependent depression at neocortical synapses. Nat. Neurosci. 15, 746-753. 10.1038/nn.3075.

Mohan, H., Verhoog, M.B., Doreswamy, K.K., Eyal, G., Aardse, R., Lodder, B.N., Goriounova, N.A., Asamoah, B., AB, B.B., Groot, C., et al. (2015). Dendritic and Axonal Architecture of Individual Pyramidal Neurons across Layers of Adult Human Neocortex. Cereb. Cortex 25, 4839-4853. 10.1093/cercor/bhv188.

Molnár, G., Rozsa, M., Baka, J., Holderith, N., Barzo, P., Nusser, Z., and Tamas, G. (2016). Human pyramidal to interneuron synapses are mediated by multi-vesicular release and multiple docked vesicles. Elife 5. 10.7554/eLife.18167.

Mukherjee, K., Yang, X., Gerber S.H., Kwon, H.B., Ho, A., Castillo, P.E., Liu, X., and Südhof, T.C. (2010). Piccolo and bassoon maintain synaptic vesicle clustering without directly participating in vesicle exocytosis. Proc. Natl. Acad. Sci. USA, 107, 6504-6509. 10.1073/pnas.1002307107.

Navarrete, M., Perea, G., Maglio, L., Pastor, J., Garcia de Sola, R., and Araque, A. (2013). Astrocyte calcium signal and gliotransmission in human brain tissue. Cereb. Cortex 23, 1240-1246. 10.1093/cercor/bhs122.

Neher, E. (2015). Merits and Limitations of Vesicle Pool Models in View of Heterogeneous Populations of Synaptic Vesicles. Neuron 87, 1131-1142. 10.1016/j.neuron.2015.08.038.

Obermayer, J., Heistek, T.S., Kerkhofs, A., Goriounova, N.A., Kroon, T., Baayen, J.C., Idema, S., Testa-Silva, G., Couey, J.J., and Mansvelder, H.D. (2018). Lateral inhibition by Martinotti interneurons is facilitated by cholinergic inputs in human and mouse neocortex. Nat. Commun. 9, 4101. 10.1038/s41467-018-06628-w.

Oliet, S.H.R., Piet, R., Poulain, D.A., and Theodosis, D.T. (2004). Glial modulation of synaptic transmission: Insights from the supraoptic nucleus of the hypothalamus. Glia 47, 258-267. 10.1002/glia.20032.

Palomero-Gallagher, N., and Zilles, K. (2019). Cortical layers: Cyto-, myelo-, receptor- and synaptic architecture in human cortical areas. Neuroimage 197, 716-741. 10.1016/j.neuroimage.2017.08.035.

Pannasch, U., Freche, D., Dallerac, G., Ghezali, G., Escartin, C., Ezan, P., Cohen-Salmon, M., Benchenane, K., Abudara, V., Dufour, A., et al. (2014). Connexin 30 sets synaptic strength by controlling astroglial synapse invasion. Nat. Neurosci. 17, 549-558. 10.1038/nn.3662.

Perkins, G.A., Tjong, J., Brown, J.M., Poquiz, P.H., Scott, R.T., Kolson, D.R., Ellisman, M.H., and Spirou, G.A. (2010). The micro-architecture of mitochondria at active zones: electron tomography reveals novel anchoring scaffolds and cristae structured for high-rate metabolism. J. Neurosci. 30, 1015-1026.

Pozzan, T., and Rizzuto, R. (2000). The renaissance of mitochondrial calcium transport. Eur. J. Biochem. 267, 5269-5273. 10.1523/JNEUROSCI.1517-09.2010.

Prume, M., Rollenhagen, A., Yakoubi, R., Sätzler, K., and Lübke, J.H. (2020). Quantitative Three-Dimensional Reconstructions of Excitatory Synaptic Boutons in the "Barrel Field" of the Adult "Reeler" Mouse Somatosensory Neocortex: A Comparative Fine-Scale Electron Microscopic Analysis with the Wild Type Mouse. Cereb. Cortex 30, 3209-3227. 10.1093/cercor/bhz304.

Rakic, P., Bourgeois, J.P., and Goldman-Rakic, P.S. (1994). Synaptic development of the cerebral cortex: implications for learning, memory, and mental illness. Prog. Brain Res. 102, 227-243. 10.1016/S0079-6123(08)60543-9.

Reynolds, E.S. (1963), The use of lead citrate at high pH as an electron-opaque stain in electron microscopy. J Cell Biol 17, 208-212. 10.1083/jcb.17.1.208.

Rizzoli, S.O., and Betz, W.J. (2004). The structural organization of the readily releasable pool of synaptic vesicles. Science 303, 2037-2039. 10.1126/science.1094682.

Rizzoli, S.O., and Betz, W.J. (2005). Synaptic vesicle pools. Nat. Rev. Neurosci. 6, 57-69. 10.1038/nrn1583.

Rizzuto, R., Bernardi, P., and Pozzan, T. (2000). Mitochondria as all-round players of the calcium game. J. Physiol. *529*, 37-47. 10.1111/j.1469-7793.2000.00037.x.

Rockland, K.S., and DeFelipe, J. (2018). Editorial: Why Have Cortical Layers? What Is the Function of Layering? Do Neurons in Cortex Integrate Information Across Different Layers? Front. Neuroanat. 12, 78. 10.3389/fnana.2018.00078.

Rollenhagen, A., Sätzler, K., Rodriguez, E.P., Jonas, P., Frotscher, M., and Lübke, J.H. (2007). Structural determinants of transmission at large hippocampal mossy fiber synapses. J. Neurosci. 27, 10434-10444. 10.1523/JNEUROSCI.1946-07.2007.

Rollenhagen, A., Klook, K., Sätzler, K., Qi, G., Anstötz, M., Feldmeyer, D., and Lübke, J.H.R. (2015). Structural determinants underlying the high efficacy of synaptic transmission and plasticity at synaptic boutons in layer 4 of the adult rat 'barrel cortex'. Brain Struct. Funct. 220, 3185-3209. 10.1007/s00429-014-0850-5.

Rollenhagen, A., Ohana, O., Sätzler, K., Hilgetag, C.C., Kuhl, D., and Lübke, J.H.R. (2018). Structural Properties of Synaptic Transmission and Temporal Dynamics at Excitatory Layer 5B Synapses in the Adult Rat Somatosensory Cortex. Front. Synaptic. Neurosci. 10, 24. 10.3389/fnsyn.2018.00024.

Rosenmund, C., and Stevens, C.F. (1996). Definition of the readily releasable pool of vesicles at hippocampal synapses. Neuron 16, 1197-1207. 10.1016/s0896-6273(00)80146-4.

Sakata, S., and Harris, K.D. (2009). Laminar structure of spontaneous and sensory-evoked population activity in auditory cortex. Neuron 64, 404-418. 10.1016/j.neuron.2009.09.020.

Sanchez-Vives, M.V., and McCormick, D.A. (2000). Cellular and network mechanisms of rhythmic recurrent activity in neocortex. Nat. Neurosci. *3*, 1027-1034. 10.1038/79848.

Saviane, C., and Silver, R.A. (2006). Fast vesicle reloading and a large pool sustain high bandwidth transmission at a central synapse. Nature 439, 983-987. 10.1038/nature04509.

Schikorski, T., and Stevens, C.F. (2001). Morphological correlates of functionally defined synaptic vesicle populations. Nat. Neurosci. 4, 391-395. 10.1038/86042.

Schikorski, T. (2014). Readily releasable vesicles recycle at the active zone of hippocampal synapses. Proc. Natl. Acad. Sci. USA 111, 5415-5420. 10.1073/pnas.1321541111.

Schneider, C.A., Rasband, W.S., and Eliceiri, K.W. (2012). NIH Image to ImageJ: 25 years of image analysis. Nat. Methods 9, 671-675. 10.1038/nmeth.2089.

Schmuhl-Giesen, S., Rollenhagen, A., Walkenfort, B., Yakoubi, R., Sätzler, K., Miller, D., von Lehe, M., Hasenberg, M., and Lübke, J.H.R. (2022). Sublamina-Specific Dynamics and Ultrastructural Heterogeneity of Layer 6 Excitatory Synaptic Boutons in the Adult Human Temporal Lobe Neocortex. Cereb. Cortex 32, 1840-1865. 10.1093/cercor/bhab315.

Schoch, S., and Gundelfinger, E.D. (2006). Molecular organization of the presynaptic active zone. Cell Tissue Res. 326, 379-391. 0.1007/s00441-006-0244-y.

Schuman, B., Machold, R.P., Hashikawa, Y., Fuzik, J., Fishell, G.J., and Rudy, B. (2019). Four Unique Interneuron Populations Reside in Neocortical Layer 1. J. Neurosci. 39, 125-139. 10.1523/JNEUROSCI.1613-18.2018.

Schuman, B., Dellal, S., Pronneke, A., Machold, R., and Rudy, B. (2021). Neocortical Layer 1: An Elegant Solution to Top-Down and Bottom-Up Integration. Annu. Rev. Neurosci. 44, 221-252. 10.1146/annurev-neuro-100520-012117.

Silver, R.A., Lübke, J., Sakmann, B., and Feldmeyer, D. (2003). High-probability uniquantal transmission at excitatory synapses in barrel cortex. Science 302, 1981-1984. 10.1126/science.1087160.

Silberberg, G., and Markram, H. (2007). Disynaptic inhibition between neocortical pyramidal cells mediated by Martinotti cells. Neuron 53, 735-746. 10.1016/j.neuron.2007.02.012.

Smith, H.L., Bourne, J.N., Cao, G., Chirillo, M.A., Ostroff, L.E., Watson, D.J., and Harris, K.M. (2016). Mitochondrial support of persistent presynaptic vesicle mobilization with age-dependent synaptic growth after LTP. Elife 5. 10.7554/eLife.15275.

Südhof, T.C. (2012). The presynaptic active zone. Neuron 75, 11-25. 10.1016/j.neuron.2012.06.012.

Südhof, T.C. (2002). Synaptotagmins: why so many? J. Biol. Chem. 277, 7629-7632. 10.1074/jbc.R100052200.

Sätzler, K., Söhl, L.F., Bollmann, J.H., Borst, J.G., Frotscher, M., Sakmann, B., and Lübke, J.H.R. (2002). Three-dimensional reconstruction of a calyx of Held and its postsynaptic principal neuron in the medial nucleus of the trapezoid body. J. Neurosci. 22, 10567-10579. 10.1523/JNEUROSCI.22-24-10567.2002.

Seeman, S.C., Campagnola, L., Davoudian, P.A., Hoggarth, A., Hage, T.A., Bosma-Moody, A., Baker, C.A., Lee, J.H., Mihalas, S., Teeter, C., et al. (2018). Sparse recurrent excitatory connectivity in the microcircuit of the adult mouse and human cortex. Elife 7. 10.7554/eLife.37349.

Schindelin, J., Arganda-Carreras, I., Frise, E., Kaynig, V., Longair, M., Pietzsch, T., Preibisch, S., Rueden, C., Saalfeld, S., Schmid, B., et al. (2012). Fiji: an open-source platform for biological-image analysis. Na.t Methods 9, 676-682. 10.1038/nmeth.2019.

Tai, X.Y., Bernhardt, B., Thom, M., Thompson, P., Baxendale, S., Koepp, M., and Bernasconi, N. (2018). Review: Neurodegenerative processes in temporal lobe epilepsy with hippocampal sclerosis: Clinical, pathological and neuroimaging evidence. Neuropathol. Appl. Neurobiol. 44, 70-90. 10.1111/nan.12458.

Tang, Y., Nyengaard, J.R., De Groot, D.M., and Gundersen, H.J. (2001). Total regional and global number of synapses in the human brain neocortex. Synapse 41, 258-273. 10.1002/syn.1083.

Testa-Silva, G., Verhoog, M.B., Linaro, D., de Kock, C.P., Baayen, J.C., Meredith, R.M., De Zeeuw, C.I., Giugliano, M., and Mansvelder, H.D. (2014). High bandwidth synaptic communication and frequency tracking in human neocortex. PLoS Biol 12, e1002007. 10.1371/journal.pbio.1002007.

Vaden, J.H., Banumurthy, G., Gusarevich, E.S., Overstreet-Wadiche, L., and Wadiche, J.I. (2019). The readily-releasable pool dynamically regulates multivesicular release. Elife 8. 10.7554/eLife.47434.

Verhoog, M.B., Obermayer, J., Kortleven, C.A., Wilbers, R., Wester, J., Baayen, J.C., De Kock, C.P.J., Meredith, R.M., et al. (2016), Layer-specific cholinergic control of human and mouse cortical synaptic plasticity. Nat. Commun. 7, 12826. 10.1038/ncomms12826.

Verstreken, P., Ly, C.V., Venken, K.J., Koh, T.W., Zhou, Y., and Bellen, H.J. (2005). Synaptic mitochondria are critical for mobilization of reserve pool vesicles at Drosophila neuromuscular junctions. Neuron 47, 365-378. 10.1016/j.neuron.2005.06.018.

von Gersdorff, H., and Borst, J.G. (2002). Short-term plasticity at the calyx of Held. Nat. Rev. Neurosci. 3, 53-64. 10.1038/nrn705.

Voigts, J., Deister, C.A., and Moore, C.I. (2020). Layer 6 ensembles can selectively regulate the behavioral impact and layer-specific representation of sensory deviants. Elife 9. 10.7554/eLife.48957.

Watanabe, S., Trimbuch, T., Camacho-Perez, M., Rost, B.R., Brokowski, B., Sohl-Kielczynski, B., Felies, A., Davis, M.W., Rosenmund, C., and Jorgensen, E.M. (2014). Clathrin regenerates synaptic vesicles from endosomes. Nature 515, 228-233. 10.1038/nature13846.

Xu, N.L., Harnett, M.T., Williams, S.R., Huber, D., O'Connor, D.H., Svoboda, K., and Magee, J.C. (2012). Nonlinear dendritic integration of sensory and motor input during an active sensing task. Nature 492, 247-251. 10.1038/nature11601.

Xu-Friedman, M.A., and Regehr, W.G. (2003). Ultrastructural contributions to desensitization at cerebellar mossy fiber to granule cell synapses. J. Neurosci. 23, 2182-2192. 10.1523/JNEUROSCI.23-06-02182.2003. 10.1371/journal.pone.0025122.

Yakoubi, R., Rollenhagen, A., von Lehe, M., Shao, Y., Sätzler, K., and Lübke, J.H.R. (2019a). Quantitative Three-Dimensional Reconstructions of Excitatory Synaptic Boutons in Layer 5 of the Adult Human Temporal Lobe Neocortex: A Fine-Scale Electron Microscopic Analysis. Cereb. Cortex 29, 2797-2814. 10.1093/cercor/bhy146.

Yakoubi, R., Rollenhagen, A., von Lehe, M., Miller, D., Walkenfort, B., Hasenberg, M., Sätzler, K., and Lübke, J.H. (2019b). Ultrastructural heterogeneity of layer 4 excitatory synaptic boutons in the adult human temporal lobe neocortex. Elife 8. 10.7554/eLife.48373.

Zagha, E. (2020). Shaping the Cortical Landscape: Functions and Mechanisms of Top-Down Cortical Feedback Pathways. Front. Syst. Neurosci. 14, 33. 10.3389/fnsys.2020.00033.

Zhao, S., Studer, D., Chai, X., Graber, W., Brose, N., Nestel, S., Young, C., Rodriguez, E.P., Sätzler, K., and Frotscher, M. (2012a). Structural plasticity of hippocampal mossy fiber synapses as revealed by high-pressure freezing. J. Comp. Neurol. 520, 2340-2351. 10.1111/j.1528-1167.2012.03469.x.

Zhao, S., Studer, D., Chai, X., Graber, W., Brose, N., Nestel, S., Young, C., Rodriguez, E.P., Sätzler, K., and Frotscher, M. (2012b). Structural plasticity of spines at giant mossy fiber synapses. Front. Neural Circuits 6, 103. 10.3389/fncir.2012.00103.

Zhou, Y.D., and Fuster, J.M. (1996). Mnemonic neuronal activity in somatosensory cortex. Proc. Natl. Acad. Sci. USA 93, 10533-10537. 10.1073/pnas.93.19.10533.

Authors contributions

Conceptualization, J.H.R.L. and A.R.; Methodology, J.H.R.L., A.R. and A.S.D.; Investigation, J.H.R.L., A.R. and A.S.D.; Writing – Original Draft, J.H.R.L., A.R. and A.S.D.; Writing – Review & Editing, J.H.R.L., A.R. and A.S.D.; Funding Acquisition, J.H.R.L. Resources, J.H.R.L.; Supervision, J.H.R.L. and A.R.

Declaration of interests

The authors disclose any financial or other interests related to the submitted work that could affect, or have the perception of affecting, the author's objectivity, or could influence, or have the perception of influencing, the content of the article.

Figures

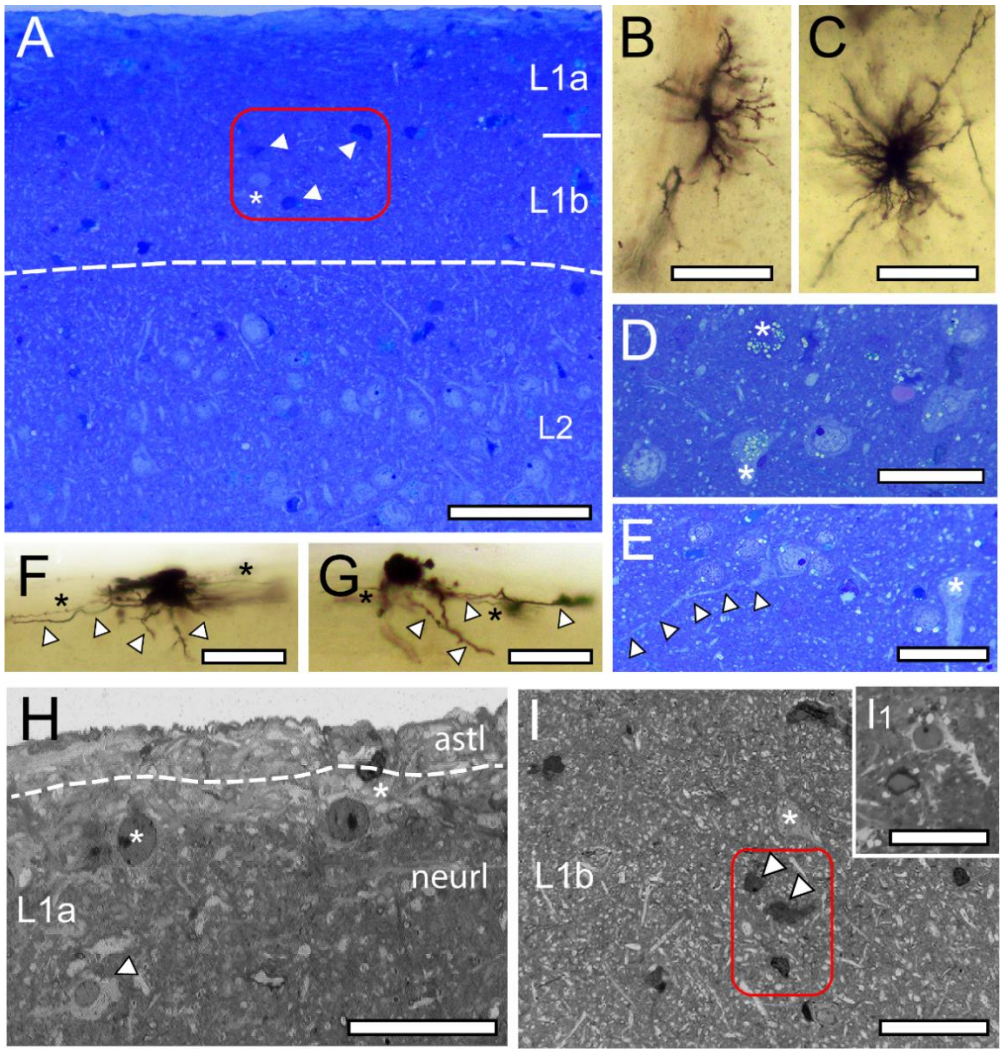

Figure 1: L1 and L2 in the human TLN as revealed in methylene-blue stained semithin sections, Golgi-impregnation and low power EM.
A, Methylene-blue stained semithin section of L1a, L1b, and L2. The cell sparse zone contains degenerating neurons (dark appearance, arrowheads in the framed area) and a cell body (asterisk in the framed area). Note the sudden increase in the density of neurons at the L1b/L2 border. Scale bar 500 µm. **B, C,** Golgi-impregnated radial astrocytes in L1a (B) and L1b (C). Scale bars 50 µm. **D,** Group of neurons in L1b containing lipofuscin granules of various shape and size (asterisks) most prominent in two of the neurons. Scale bar 50 µm. **E,** Putative CR-cell identifiable by its long horizontally oriented dendrite (marked by asterisks) and an inverted putative GABAergic interneuron (asterisk) in L1b. Scale bar 50 µm. **F, G,** Golgi-impregnated CR-Cells in L1a with the characteristic horizontal orientation of dendrites (arrowheads) and axons (asterisks). Scale bars 50 µm. **H,** EM micrograph of L1a (astrocytic layer, astl) underneath the pial surface. Note the abrupt transition (indicated by the dashed line) to a neuropil (neurl) containing two putative CR-cells (asterisks), a reactive microglial cell (arrowhead), and dendrites and synapses. Scale bar 25 µm**. I,** EM micrograph of L1b containing thousands of dendritic profiles, a putative GABAergic interneuron (framed area, asterisk) but also degenerating neurons (framed area, arrowheads) and a reactive microglia (I1) Scale bar 50 µm**.**

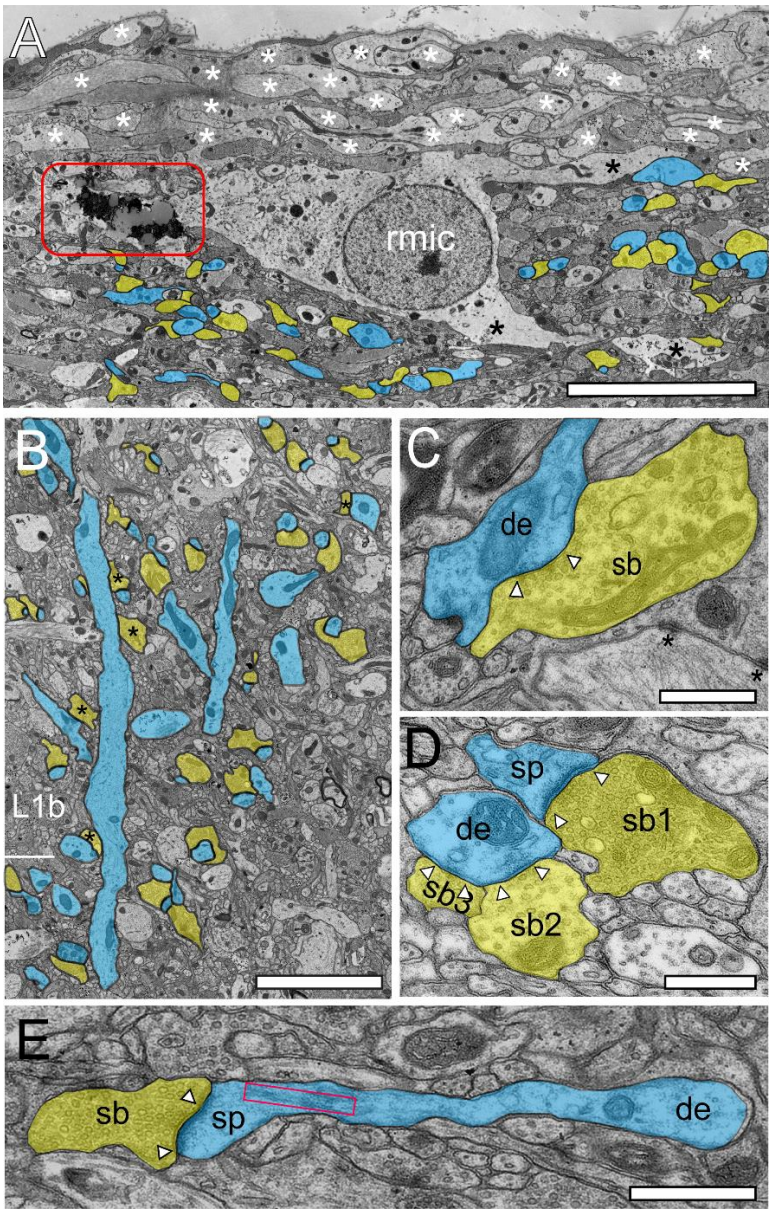

Figure 2: Structural and synaptic organization of L1 in the human TLN as revealed by EM.
A, Superficial part of L1a composed of a dense network of fine astrocytic processes (asterisks). In the reactive microglial cell (rmic) so-called lipofuscin granules (framed area) were observed. Below the astrocytic network synaptic complexes gradually increased (highlighted in blue for target structures, yellow for SBs). Scale bar 10 µm. **B,** Two apical dendrites (blue) traversing L2 with beginning terminal tuft dendrites in L2 and L1 contacted by SBs (transparent yellow); some of which are putatively GABAergic terminating on the dendritic shaft (asterisks). Scale bar 2.5 µm. **C,** Large GABAergic SB (sb, transparent yellow) identifiable by the small-sized ovoid SVs and the less prominent PSD (arrowheads) synapsing on a dendritic shaft (de, transparent blue) in L1b. **D,** Three SBs in L1a (sb1-sb3, transparent yellow) located on a dendritic spine (sp, transparent blue) and a neighboring dendritic shaft (sh, transparent blue). Note that sb1 is excitatory as indicated by the larger round SVs with a prominent AZ whereas sb2 and sb3 are putative inhibitory terminals identified by smaller ovoid SVs and the lack of a prominent PSD. **E,** Elongated spine (sp) emerging from a small caliber dendrite (de, transparent blue) receiving input from a small-sized SB (sb, transparent yellow). Note the large, elongated spine apparatus (framed area). Scale bar in C-E 0.5 µm. In graphs C-E AZs are marked by arrowheads.

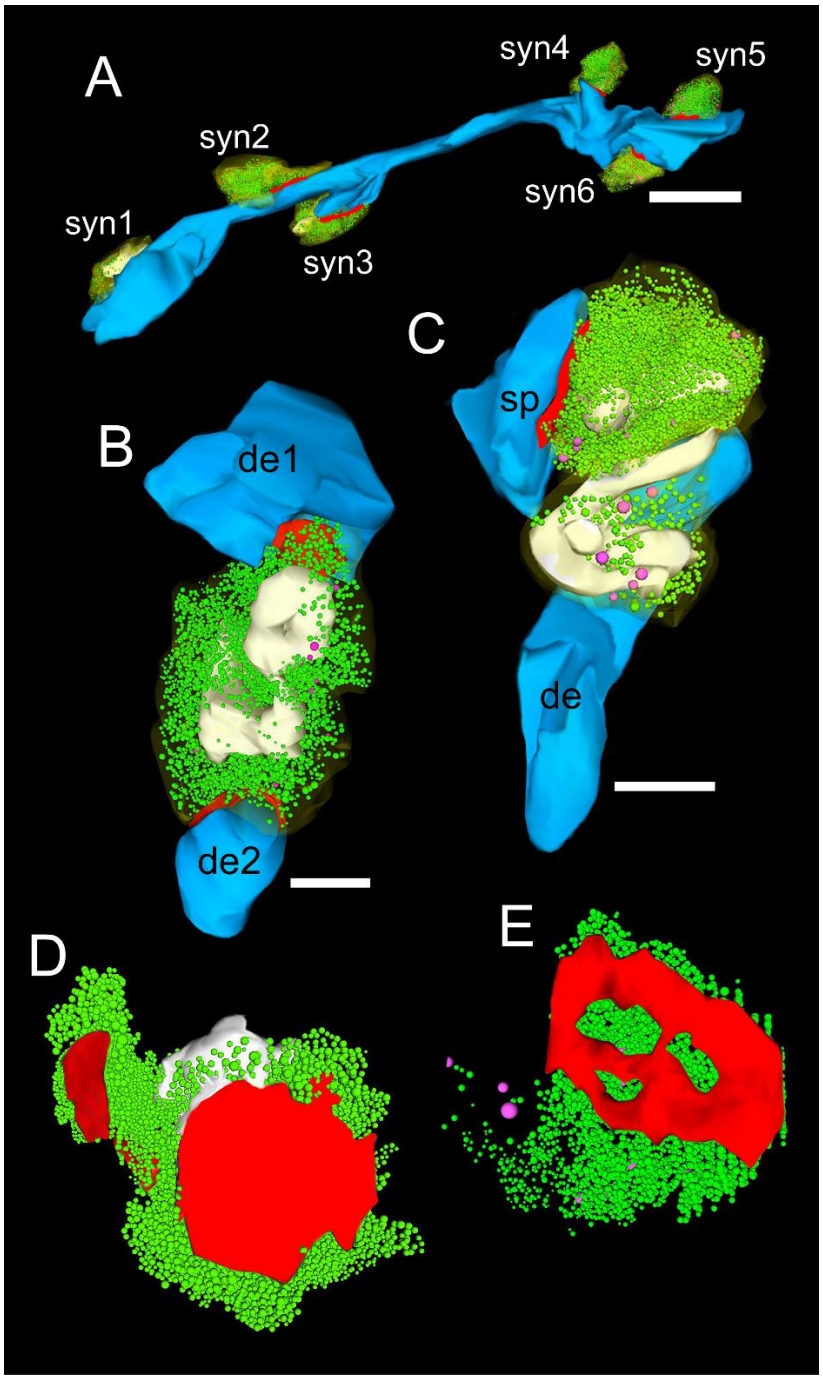

Figure 3: 3D-volume reconstructions of SBs and vesicle pools in L1a and L1b of the human TLN. **A-D,** Here, all SBs are colored in transparent yellow. Subelements: PreAZs (red), SVs (green), DCVs (magenta), mitochondria (white). The postsynaptic target structures are given in blue **A,** Six SBs (sb1-sb6) terminating at different locations on a dendritic segment in L1b, two of which (syn3 and syn4) were located on spines, the remaining on the dendritic shaft. Scale bar 1 µm. **B,** Large SB terminating on two dendritic segments of different shape and size (de1, de2) in L1a. **C,** SB synapsing on a dendrite (de) and spine (sp) in L1b containing several mitochondria associated with the pool of SVs. **D, E,** 3D-volume reconstructions of the total pools of SVs (green dots). Note the different shape and size of the PreAZs (red) with either a non-perforated macular (D) or perforated (E) appearance and the comparably large total pool size. Note the large DCVs intermingled with the pool of SVs.

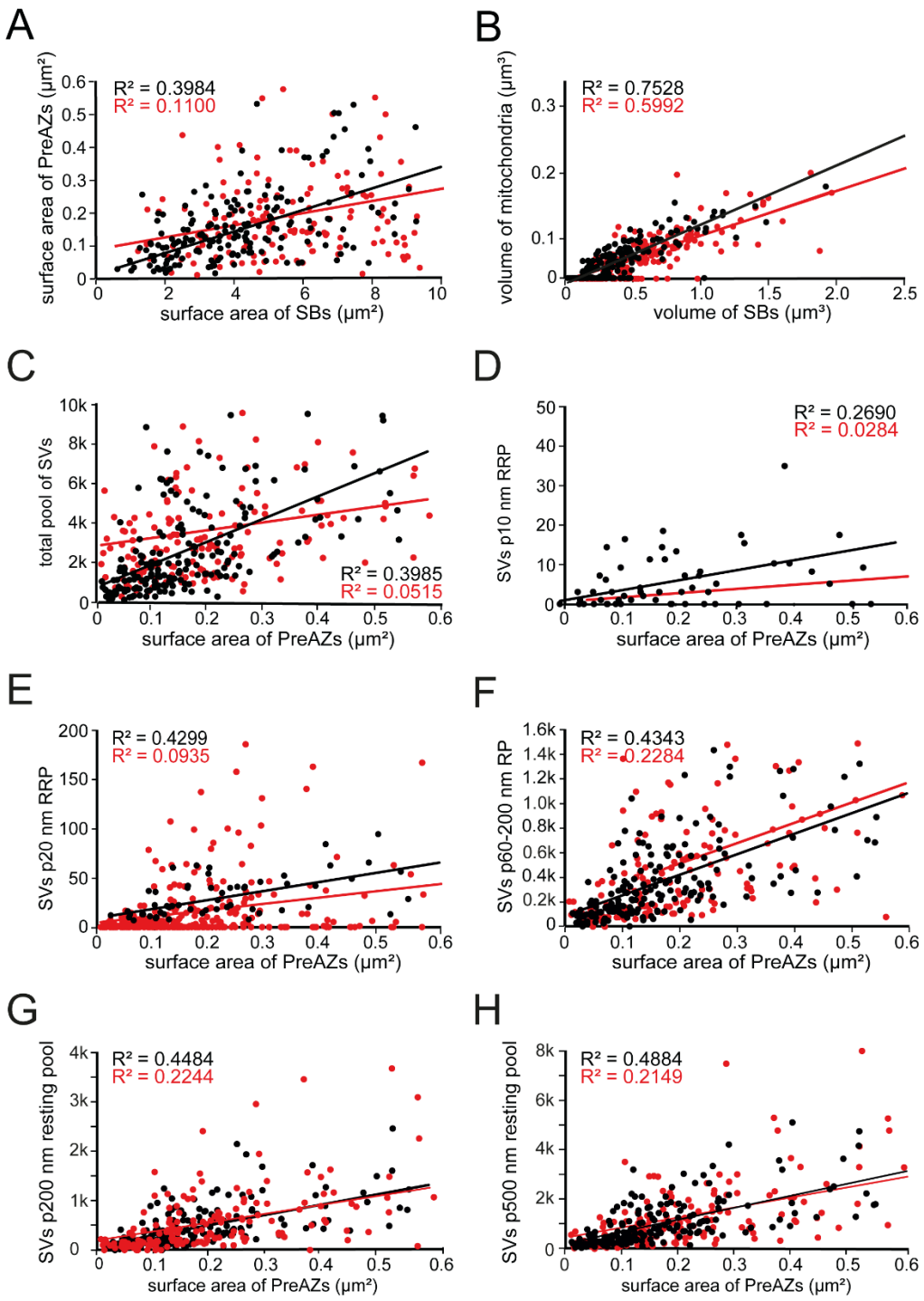

Figure 4: Correlation plots for structural and synaptic parameters characterizing L1 SBs. Correlation plots showing the strength of correlations between structural and synaptic parameters (Source Data 2). Correlations dots and regression lines for L1a are given in black and that for L1b in red. **A,** Surface area of SBs vs. surface area of PreAZ; **B,** Volume of SBs vs. volume of mitochondria; **C,** Surface area of PreAZs vs. total pool of SVs; **D,** Surface area of PreAZs vs. p10 nm RRP; **E,** Surface area of PreAZs vs. p20 nm RRP; **F,** Surface area of PreAZs vs. p60-p200 nm RP; **G,** Surface area of PreAZs vs. p200 nm resting pool; **H,** Surface area of PreAZs vs. p500 nm resting pool.

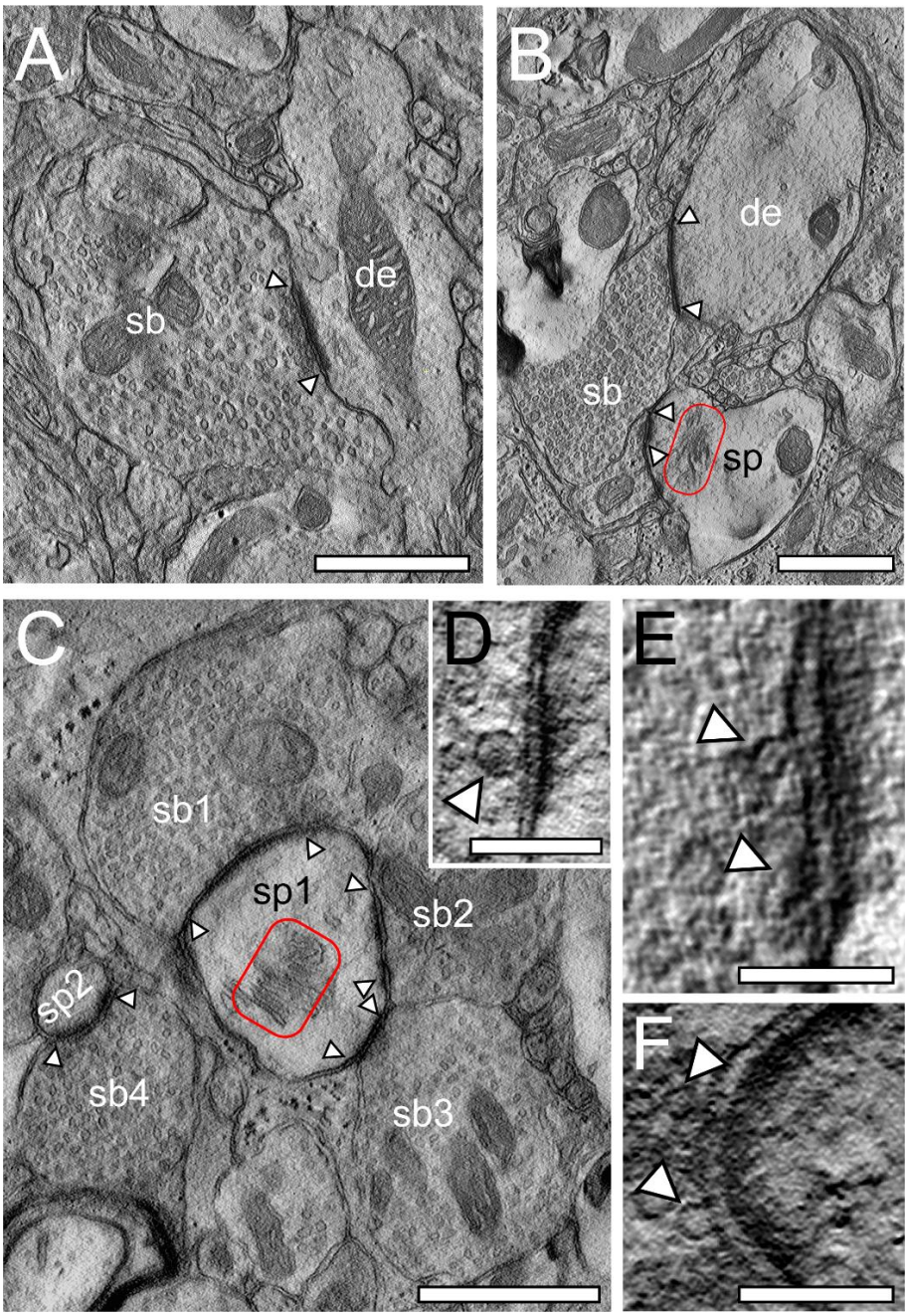

Figure 5: EM tomography of SBs in L1a and L1b in the human TLN.
A, Large SB (sb) terminating with a single AZ (arrowheads) on a terminal tuft dendritic shaft (de) in L1a. **B,** SB (sb) synapsing on a stubby spine (sp) with a prominent spine apparatus (framed area) and a thick dendritic segment (de) in L1b. Scale bars 1 µm. **C,** Large mushroom (sp1) and a small spine head (sp2) receiving input from three SBs (sb1, sb2, sb3) and a single SB (sb4) in L1b. Note the large AZs (arrowheads) and the prominent spine apparatus (red framed area) in the mushroom spine. Scale bar 0.5 µm. **D, E, F,** High-power images of 'docked' SVs (arrowheads) taken from a tilt-series through an individual PreAZ at a L1a spine SB. Note the so-called omega-shaped bodies in (E, F) pointing to the already opening and release of glutamate quanta. Scale bars 0.1 µm.

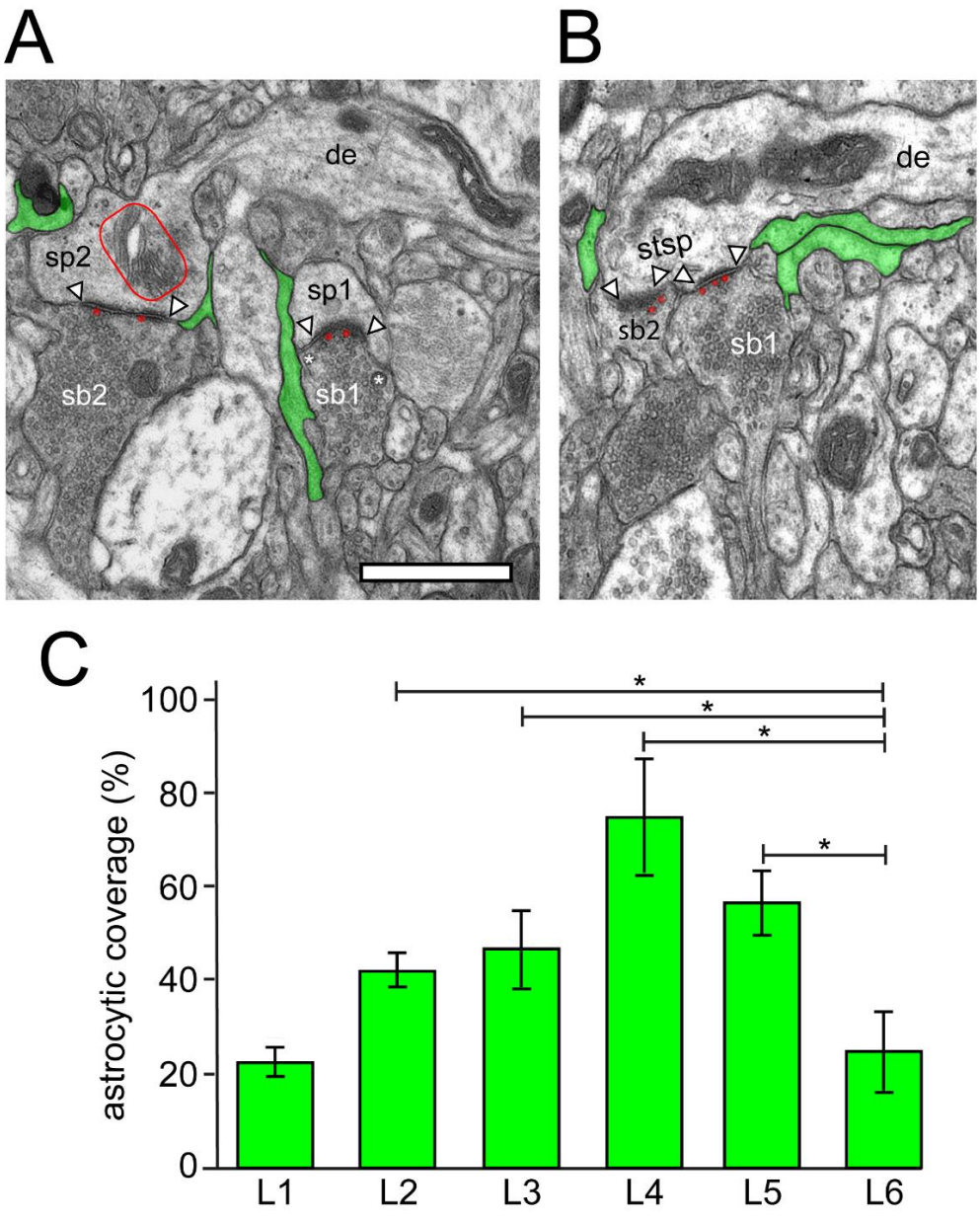

Figure 6: Astrocytic coverage of synaptic complexes in the human TLN.
A, EM micrograph of two adjacent SBs (sb1, sb2) terminating on two spines (sp1, sp2) in L1a. Sp2 contained a prominent spine apparatus (framed area), sb1 two DCVs (asterisks). Note that both synaptic complexes were only partially ensheathed by fine astrocytic processes (transparent green) reaching the AZs only on one side. In both synaptic complexes two 'docked' SVs (transparent red) at the PreAZs were found. Scale 0.25 µm. **B,** Stubby spine (stsp) receiving two SBs (sb1, sb2) in L1b. Here, fine astrocytic processes (transparent green) were found close to the two synaptic complexes but never reached the synaptic cleft. Note also the 'docked' SVs (transparent red) pointing to multivesicular release. In both images the AZs are marked by arrowheads. Scale bar 0.25 µm. **C,** Bar histogram showing the percentage (mean ± SD) of the volumetric fraction of astrocytic processes to the total volume in L1 to L6. Values for L6 are taken from Schmuhl-Giesen et al. 2022. The horizontal bars indicate significant differences between cortical layers *: $p < 0.05$ (Source Data 4).

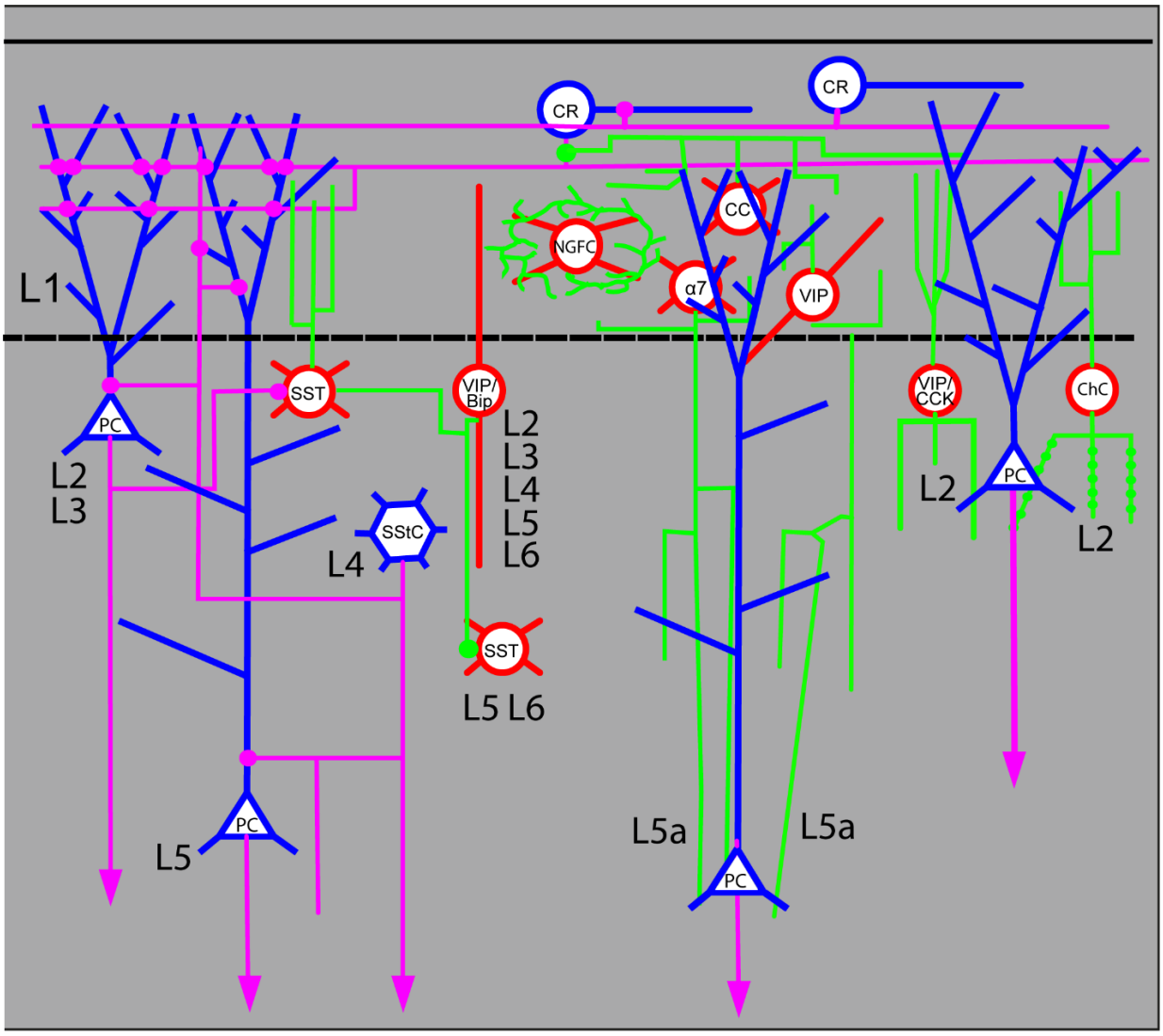

Figure 7: Schematic drawing of the possible wiring of L1 in the human TLN.
The possible neuronal and synaptic organization of neocortical L1 in humans modified and based on findings from rat neocortex (reviewed by Schuman et al. 2021). The dendritic domain of excitatory neurons is given in blue, the axonal projection and connectivity in magenta and that of different GABAergic interneurons in red and brown, respectively. Furthermore, a subpopulation of persistent CR-cells is illustrated in the diagram.
Abbreviations: α7: nicotinic receptor-expressing interneuron; CanC: canopy cell; ChC: chandelier cell; L: layer; NGFC: neurogliaform cell; PC: pyramidal cell; SST: somatostatin containing interneuron; VIP: vasoactive intestinal peptide-expressing interneuron; VIP/Bip: vasoactive intestinal peptide–expressing bipolar interneuron; VIP/CCK: cholecystokinin- and vasoactive intestinal peptide-expressing interneuron.

Table 1: Comparative quantitative analysis of various structural and synaptic parameters in L1 of the human TLN.

	Layer	Mean ± SD	Median	IQR	CV	Variance	Skewness
		Synaptic boutons					
Surface area (µm²)	L1	5.48 ± 1.40	5.75	2.20	0.26	1.96	0.21
	L1a	4.58 ± 1.13	4.27	2.20	0.25	1.28	1,13
	L1b	6.39 ± 1.08	5.87	1.97	0.17	1.17	1.66
Volume (µm³)	L1	0.50 ± 0.19	0.38	0.33	0.39	0.04	0.13
	L1a	0.41 ± 0.21	0.49	0.41	0.50	0.04	0.64
	L1b	0.58 ± 0,17	0.48	0.31	0.30	0.03	1.71
		Active zones					
PreAZ surface area (µm²)	L1	0.20 ± 0.06	0.22	0.08	0.30	0.01	-1.53
	L1a	0.18 ± 0.08	0.22	0.14	0.43	0.00	-1.70
	L1b	0.22 ± 0.04	0.22	0.08	0.18	0.00	0,00
PSD surface area (µm²)	L1	0.22 ± 0.07	0.23	0.12	0.32	0.00	-0.91
	L1a	0.21 ± 0.10	0.23	0.19	0.47	0.01	-1.02
	L1b	0.22 ± 0.05	0.22	0.09	0.20	0.00	0.33
Cleft width (nm)	L1	L: 21.75 ± 2.72 C: 29.63 ± 2.36	L: 22.20 C: 29.73	L: 2.88 C: 3.19	L: 0.13 C: 0.08	L: 7.40 C: 5.56	L: -1.03 C: -0.96
	L1a	L: 20.17 ± 2.85 C: 29.06 ± 3.48	L: 21.44 C: 29.17	L: 5.25 C: 6.95	L: 0.14 C: 0.12	L: 8.10 C: 12.08	L: -1.61 C: -0.14
	L1b	L: 23.34 ± 1.70 C: 30.19 ± 0.92	L: 22,49 C: 30,19	L: 3.06 C: 1.84	L: 0.07 C: 0,03	L: 2,88 C: 0,85	L: 1.69 C: 0,00
		Mitochondria					
Volume (µm³)	L1	0.04 ± 0,02	0.04	0.03	0.35	0.00	-0.31
	L1a	0.04 ± 0,02	0.04	0.04	0.50	0.00	0.00
	L1b	0.05 ± 0,01	0.04	0.02	0.25	0.00	1.73
% to the total volume	L1	7.21 ± 1.10	7.56	1.81	0.15	1.21	-1.13
	L1a	7.18 ± 1.60	8.06	2.81	0.22	2.56	-1.73
	L1b	7.23 ± 0.68	7.17	1.35	0.09	0,46	0.42
		Synaptic vesicles					
Total number of SVs	L1	3430.97 ± 1773.77	3675.96	3386.86	0.52	3146276.00	-0.31
	L1a	2958.62 ± 1940.51	2980.76	3880.83	0.66	3765578.00	-0.05
	L1b	3903.32 ± 1852.23	4371.16	3614.75	0.47	3430758.00	-1.06
Volume (µm³)	L1	0.03 ± 0.02	0.03	0.03	0.60	0.00	0.94
	L1a	0.02 ± 0.01	0.02	0.02	0.50	0.00	0.00
	L1b	0.04 ± 0.02	0.04	0.04	0.50	0.00	0.00
Vesicle diameter (nm)	L1	25.03 ± 5.67	26.36	10.38	0.23	32.13	-0.31
	L1a	23.33 ± 5.27	25.88	9.56	0.23	27.74	-1.67
	L1b	26.73 ± 6.63	28.25	12.99	0.25	43.93	-0.98
		Pool sizes of SVs					
Putative RRP p10 nm from the PreAZ	L1	3.60 ± 4.24	2.10	6.98	1.18	17.99	1.17
	L1a	5.90 ± 5.05	6.11	10.10	0.86	25.53	-0.18
	L1b	1.29 ± 1.87	0.41	3.41	1.44	3.49	1.65
Putative RRP p20 nm from the PreAZ	L1	19.05 ± 17.23	17.17	29.37	0.90	296.86	0.67
	L1a	25.04 ± 21.09	24.82	42.18	0.84	444.82	0.05
	L1b	13.07 ± 13.78	9.52	26.86	1.05	189.80	1.08
Putative RP 60-200 nm from the PreAZ	L1	463.00 ± 283.82	512.65	554.39	0.61	80553.57	-0.19
	L1a	390.12 ± 286.89	335.05	565.79	0.74	82304.11	0.83
	L1b	535.88 ± 321.16	690.25	584.03	0.60	103145.30	-1.66
Putative resting pool > 200 nm from the PreAZ	L1	2896.50 ± 1435.93	3120.39	2698.41	0.50	2061880.00	-0.38
	L1a	2515.02 ± 1588.99	2662.80	3167.65	0.63	2524880.00	-0.41
	L1b	3277.97 ± 1480.96	3577.98	2915.99	0.45	2193254.00	-0.87

Summary of different structural parameter measurements (bold) from the detailed 3D-volume reconstructions of SBs in L1, separated for sublaminae. Values are presented as mean, SD, median, IQR, CV, skewness, and variance for each parameter for all patients studied. #: Values with skewness > 3 indicate a non-normal distribution. Abbreviations: L: lateral; and C: central (Source Data 2).

Table 2: 'Docked SVs' in L1a and L1b of the human TLN.

	Layer	Mean ± SD	Median	IQR	CV	Skewness	Variance
Number of docked vesicles	**L1** (n=360 SVs)	3.56 ± 1.36	4.00	3.00	0.38	-0.07	1.85
	L1a	3.71 ± 1.38	4.00	3.00	0.37	-0.16	1.89
	SBs on dendritic shafts (n=91 SVs)	3.64 ± 1.47	4.00	3.00	0.40	-0.08	2.16
	SBs on dendritic spines (n=98 SVs)	3.77 ± 1.31	4.00	2.00	0.35	-0.24	1.70
	L1b	3.42 ± 1.34	3.00	3.00	0.39	0.02	1.80
	SBs on dendritic shafts (n=87 SVs)	3.48 ± 1.45	3.00	3.00	0.42	0.04	2.09
	SBs on dendritic spines (n=84 SVs)	3.36 ± 1.25	3.00	2.50	0.37	-0.07	1.57

Summary of the number of 'docked' SVs in L1, separately for both sublaminae as well as for the different target structures dendritic shafts vs. dendritic spines. Mean ± SD, median, IQR, CV, skewness, and variance are given for each parameter in all patients studied (Source Data 3).

Supplemental Information

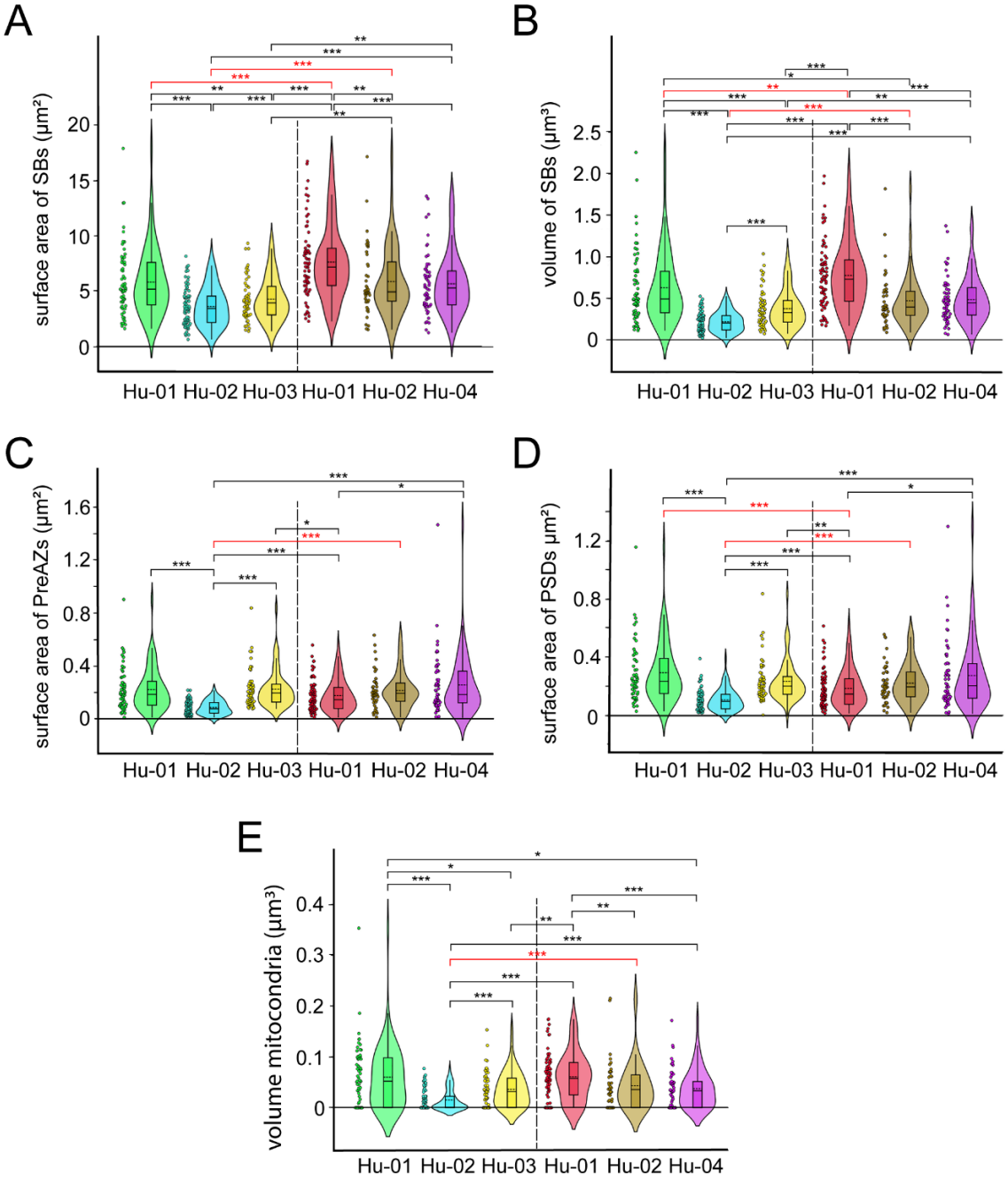

Supplemental Figure 1: Box plots of various structural parameters in L1 of the human TLN
Data distributions for each patient are indicated by the medians (horizontal bars), IQRs (framed areas), minimum and maximum (vertical lines) for the distribution of: A, Surface area of SBs; B, Volume of SBs; C, Surface area of PreAZs; D, Surface area of PSD; E, Volume of mitochondria. Significant differences between different patients are indicated by asterisks. Note that several structural parameters are significantly different. The significant bars highlighted in red indicate significant differences between sublaminae L1a and L1b in the same patient. *: $p < 0.05$; **: $p < 0.01$; ***: $p < 0.001$ (Source Data 2).

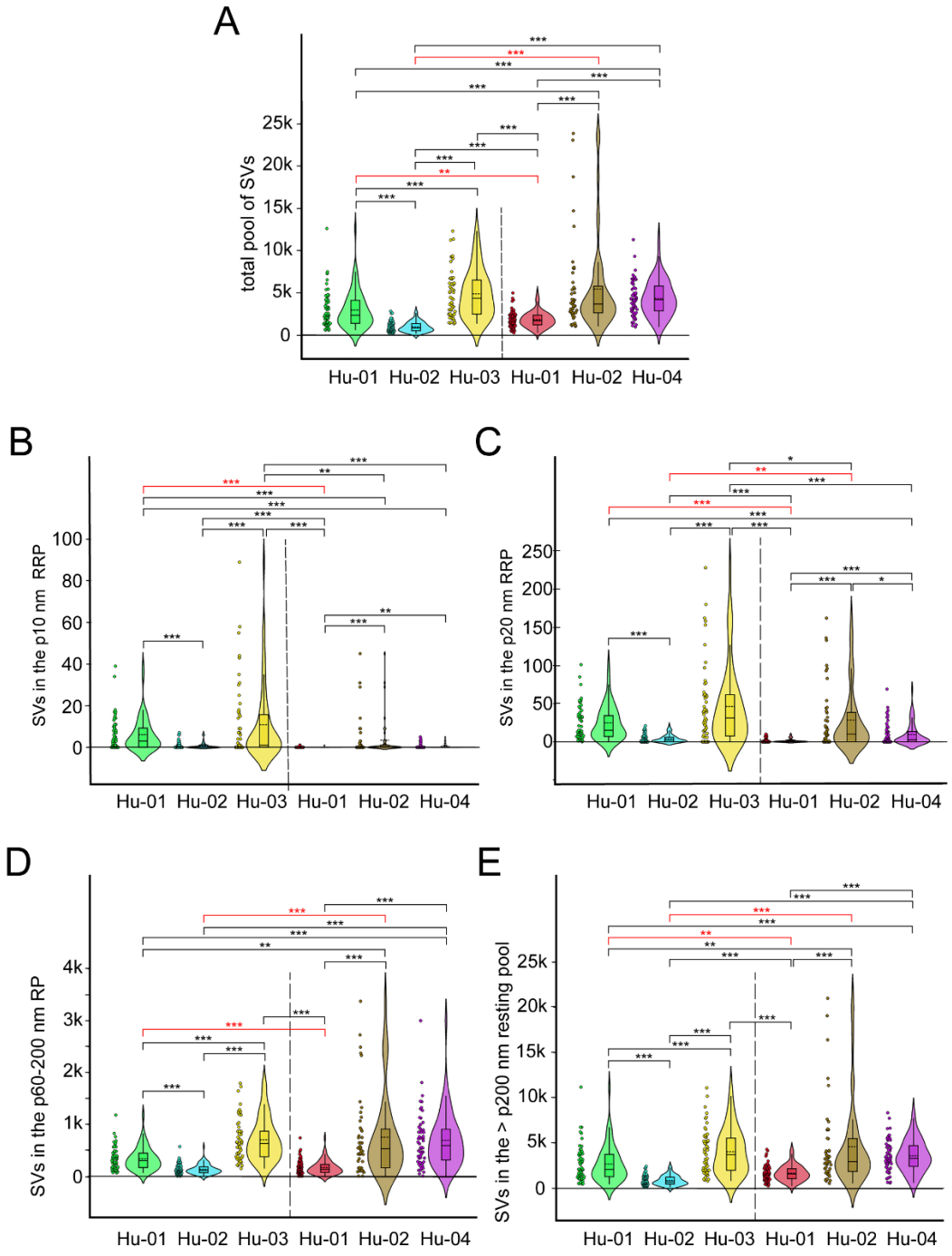

Supplemental Figure 2: Box plots of various synaptic parameters in L1 of the human TLN
Data distributions for each patient are indicated by the medians (horizontal bars), IQRs (framed areas), minimum and maximum (vertical lines) for the distribution of: **A,** Total pool of SVs; **B,** SVs in the p10 nm RRP; **C**, SVs in the p20 nm RRP; **D**, SVs in the p6-200 nm RP; **E**, SVs in the > p200 nm resting pool; Note that several structural parameters are not significantly different. The significant bars highlighted in red indicate significant differences between sublaminae L1a and L1b in the same patient. *: $p < 0.05$; **: $p < 0.01$; ***: $p < 0.001$ (Source Data 2).

Supplemental Table 1: Patient's identity and medical background

Patient identity and medical history	Gender	Age (years)	Age at epilepsy onset (years)	Histo-Pathology	Antiepileptic drugs (pre-op)	Number of SBs recon-structed
Hu_01	♂	52	20	AHS	LEV, OXC, Perampanel	L1a: 63; L1b: 70
Hu_02	♀	27	16	Micro- and Astrogliosis	LEV, Topiramat, Zebinix	L1a: 72; L1b: 45
Hu_03	♀	65	1	Hippocampal sclerosis	LEV, LTG, Primidone	L1a: 55
Hu_04	♀	24	_	TLE	_	L1b: 56

AHS: Ammon's horn sclerosis; BAZ: Brivaracetam CBZ: Carbamazepine; CLB: Clobazam; ESL: Eslicarbazepin; GGL: Ganglioglioma; LEV: Levetiracetam; LTG: Lamotrigine; OXC: Oxcarbazepin; ZONI: Zonisamide.